Title

Experimental study of three-dimensional CO2-water drainage and fracture-matrix interactions in fractured porous media

Authors

Chang, Chun
Kneafsey, Timothy J
Zhou, Quanlin

Publication Date

2021-09-01

DOI

10.1016/j.advwatres.2021.104008

Peer reviewed

Experimental Study of Three-Dimensional CO_2-Water Drainage and Fracture-Matrix Interactions in Fractured Porous Media

Chun Chang*, Timothy J. Kneafsey, Quanlin Zhou

Energy Geosciences Division, Lawrence Berkeley National Laboratory, University of California, Berkeley, California, CA94720, USA.

*Corresponding author. *E-mail address*: chunchang@lbl.gov

Highlights

1. We imaged 3-D CO_2-water drainage in vertically stacked matrix-fracture columns that are different from classic core-flood settings.
2. Capillary continuity in the fracture was key to water drainage and CO_2 invasion in the matrix.
3. Fracture water saturation and capillary continuity were enhanced by the non-uniform fracture capillary pressure and countercurrent flow across the fracture-matrix interface.

Abstract: Estimation of CO_2 storage capacity in fractured porous reservoirs requires a better understanding of the CO_2-water flow fundamentals in fracture-matrix systems. There are few core-flood experiments on three-dimensional CO_2-water drainage in a fracture-matrix system, yet none have examined the impacts of the capillary continuity of fractures and fracture-matrix interactions. In this study, twelve drainage experiments were conducted in four fracture-matrix columns, each comprising a vertical stack of a cylindrical rock core, a filter paper serving as an analog to a horizontal fracture, and a ceramic plate. The core sample was surrounded by open space at the top and circumferential sides to model fractures, allowing for 3-D CO_2-water drainage in the rock core and displaced water draining across the horizontal fracture. X-ray computed tomography was conducted to visualize the dynamic invasion/drainage processes in four rock core samples showing contrasts in anisotropy, permeability, and heterogeneity. Experimental results show (1) the equilibrium CO_2 saturations in the rock matrix vary from 0.10 to 0.60 at controlled capillary pressures up to 200 kPa, (2) the CO_2 saturations in the matrix increase with water saturation in the horizontal fracture resulting in better capillary continuity for water to drain across the fracture, and (3) the fracture water saturation can be enhanced by the non-uniform fracture capillary pressure and countercurrent flow of CO_2 and water across the fracture-matrix interface. In the case of high fracture water saturation, matrix CO_2 saturation largely depends on matrix anisotropy and heterogeneity. The core-scale experimental results contribute to understand the fracture-matrix interactions and CO_2 storage efficiency in fractured porous media.

Keywords: Geological carbon storage, Fractured porous media, Two-phase flow, Core-flooding, X-ray CT, Fracture-matrix interactions

1. Introduction

Two-phase flow characteristics of CO_2-water in subsurface fractured media are of great interest as fractured carbonate and sandstone reservoirs are increasingly considered as potential geological CO_2 sequestration (GCS) and simultaneous oil recovery locations because of their ubiquity in sedimentary basins (Agada et al., 2016). In saline aquifers, GCS in sandstone formations is also considerably influenced by the presence of fractures and faults, as reported from the currently world's largest onshore CO_2 storage site, the Krechba site within the In Salah gas field (Iding & Ringrose, 2010). It is also noted that fractures are a major source of uncertainty in subsurface media, and the existence of unidentified fracture networks should be incorporated with well-understood CO_2-water flow behaviors for risk analysis of storage projects (Narr et al, 2006; March et al., 2018).

The bulk of CO_2 storage in fractured reservoirs occurs in the interconnected pore volumes of the rock matrix because of its high porosity. Peters and Klavetter (1988) reported the fracture porosity three to five orders of magnitude lower than the matrix porosity, although the preferential and fast flow of injected CO_2 is expected to occur in fractures due to the overall higher fracture permeability than that of the (porous) rock matrix. CO_2 invasion into the rock matrix from fractures and brine drainage through matrix blocks are critical in establishing CO_2 storage in fractured reservoirs. Capillarity and gravity are usually major forces affecting the CO_2 invasion from fractures to the matrix, whereas viscous force may be more relevant in the near-well region, where large pressure gradients may impose viscous displacement inside the matrix blocks (March, 2018). Diffusion of dissolved CO_2 from fractures into the rock matrix could also be

pronounced, however, it may take a longer time for CO_2 diffusion to contribute to storage capacity (Pruess et al., 1990; Zhou et al., 2017).

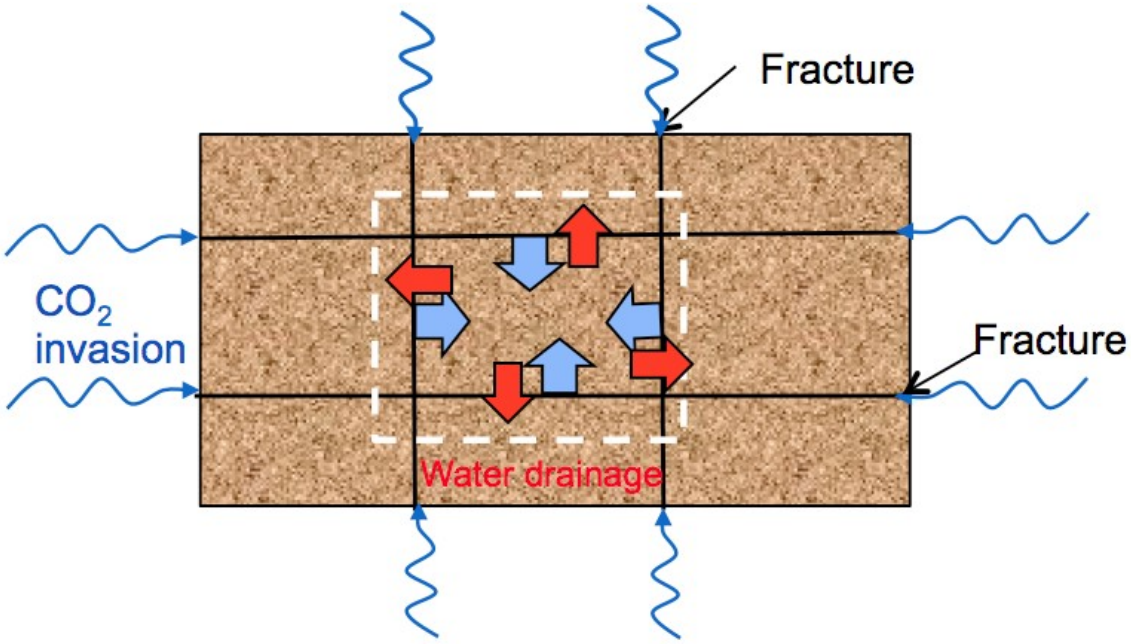

Figure 1. Conceptual model of CO_2-water displacement through a fracture-matrix system. After injection, water desaturation in the fractures occurs first, followed by CO_2 invasion into the blocks (e.g., the central block marked by the white dotted line). The thin blue arrows indicate the preferential CO_2 flow in the fractures, while the thick blue arrows refer to the subsequent CO_2 invasion from fractures to matrix. The red arrows represent water drainage in neighboring matrix across portions of the fractures that may retain water to an extent that water drainage across the fractures is available.

Figure 1 presents the conceptual model of CO_2-water flow in a fractured system dominated by capillarity. After CO_2 injection, water desaturation in the largest flow pathways (fractures) occurs first, followed by CO_2 invasion into matrix blocks (e.g., the

77 central block marked by the white dotted line). The invasion of CO_2 from fractures to
78 matrix can only occur when water drainage from one matrix block to its neighboring
79 blocks occurs. Countercurrent flow of CO_2 and water across the same fracture could
80 happen in any direction, when (1) water is retained in portion of the fracture to an extent
81 that water drainage across the fracture is available (red arrow in Figure 1), and (2) the
82 capillary entry pressure of the water-wet matrix (or water-wet portion of the matrix) is
83 lower than the capillary pressure in the fractures (thick blue arrows in Figure 1). For
84 some of the fractured carbonates that may be either mixed wet or oil wet, CO_2 could be
85 the wetting phase and spontaneously imbibing the rock matrix (Al-Menhali et al., 2016;
86 Arif et al., 2017). Gravity may facilitate water bridging in horizontal fractures and favor
87 water drainage between blocks (Horie et al., 1990). Extensive core-flood experiments
88 have been conducted to investigate (1) the capillary pressure vs. saturation characteristics
89 of fractures under in-situ conditions using X-ray computed tomography (CT) scanning
90 (Reitsma and Kueper, 1994; Bertels et al., 2001, Huo and Benson, 2016), (2) the fracture-
91 matrix transfer functions, which are the backbone of dual-porosity formulation in
92 modeling of fluid flow in fractured porous media (Beckner et al., 1987; Gautam and
93 Mohanty, 2004; Lim and Aziz, 1995; Rangel-German and Kovscek, 2005, 2006; Rangel-
94 German et al., 2006; Penuela et al., 2002; Tao et al., 2019), and (3) the potential capillary
95 continuity between matrix blocks established by liquid bridges across open fractures with
96 varying wettability surfaces (Aspenes et al., 2008; Dejam and Hassanzadeh, 2010; Fernø
97 et al., 2011). Common to all the studies above is that two-phase flow was prohibited
98 through the sample circumferential surface because confining pressure was applied to the
99 core, allowing displacement to occur only along the long-axis from inlet to outlet. To the

100 best of our knowledge, there are few core-flood experiments on three-dimensional CO_2-
101 water drainage in a fracture-matrix system, and none have examined the impacts of the
102 capillary continuity of fractures and fracture-matrix interactions.

103 In this study, we conducted water drainage experiments in four fracture-matrix
104 columns to investigate the 3-D CO_2-water drainage across a horizontal fracture between
105 two neighboring matrix blocks. Each column was composed of a water-wet rock core, a
106 filter paper that provides an analog for horizontal fracture, and a water-wet ceramic plate
107 that was located at the bottom of the vertical stack. Four rock core samples (5 cm
108 diameter and ~10 cm long) with contrasts in foliation anisotropy, permeability, and
109 heterogeneity were used as the upper matrix block. Two types of ceramic plates were
110 selected as the lower matrix block to allow control of the capillary pressure applied to the
111 upper matrix block, without changing the hydraulic continuity downstream of the
112 horizontal fracture. The changes in fracture water saturation (thus the capillary continuity
113 and water relative permeability) at applied capillary pressures (P_c), the displacement
114 efficiency and the drainage time scale in the upper matrix block were investigated
115 through frequent X-ray CT scans.

116 ## 2. Material and methods

117 ### 2.1 Rock cores

118 Four rock core samples, with a diameter of 5.0 cm and a length varying from 9.5 to
119 10 cm, were used for the stacked-column tests. Samples #1 and #2 were cut from a
120 Carbon Tan sandstone block from outcropped Late Cretaceous formation, Utah, US, with
121 bedding layers orthogonal and parallel to the long axis (Kocurek Industries, TX). Their

122 average porosities were calculated from CT images and Eq. (1) as 0.16 and 0.15,
123 respectively. For each sample, four thin disks (5.0 cm diameter and 1.0 cm thickness)
124 were oven-dried and weighed, followed by saturating with deionized (DI) water under -
125 101kPa for over 6 hours. The water-saturated disks were then weighed, and the porosity
126 of each disk was measured gravimetrically. The measured porosities for Samples #1 and
127 #2 is 0.16 ± 0.0012 and 0.15 ± 0.0011, similar to the values obtained from CT images of
128 10 cm long cores. The absolute air permeabilities of Sample #1 and #2 were measured as
129 46 and 51 mD. More details on the permeability measurements of the samples can be
130 seen in the supporting information (Figure S1 of SI). Sample #3 was cut from a Kentucky
131 sandstone block (Virginia, US) with the long axis parallel to the bedding layers (Kocurek
132 Industries, TX). The porosity of Sample #3 measured from CT images is 0.14, while the
133 value from thin discs is 0.13± 0.0012. The air permeability is measured as 6.67 mD.
134 Sample #4, a Duperow dolostone, was obtained from a depth of 1260 m from the
135 Wallewein 22-1 well, a planned injection well for a CO_2 geological storage test at Kevin
136 Dome, Montana. The porosity of Sample #4 was measured by water saturating under -
137 101 kPa for 3 days, until the time-lapse CT images showed a constant porosity at 0.042±
138 0.0012. The absolute air permeability for the sample was measured at 0.17 mD. Table 1
139 lists the size, porosity and permeability measurements on the four core samples. Figure
140 2a depicts the profile (by blue curve) of the average porosity of 0.625 mm horizontal
141 slices derived from X-ray CT scans along the long-axis, with the background image
142 showing the porosity distribution of a 2-D cross section along the central axis. The
143 porosity distribution of Sample #4 by the X-ray CT image indicates (1) a low-porosity
144 (0.02 to 0.04) portion “P1” (0-35 mm) with two tight fractures, (2) a low-porosity (0.02

145 to 0.04) portion “P2” (35 to 55 mm) with one open fracture, and (3) a higher porosity
146 (0.04 to 0.06) portion “P3” (55 to 95 mm) with one tight fracture. These fractures are
147 marked by the white arrows in Figure 2a and further discussed in Section 3.3. The
148 absolute water permeability of each sample in Table 1 was converted from air
149 permeability measurements considering Klinkenberg effect (Klinkenberg, 1941; Jones
150 and Owens, 1980). To quickly represent the sample characteristics, we use high (H),
151 medium (M), and low (L) permeability, and bedding/fracture orthogonal (O) to or parallel
152 (P) to the water drainage path to redefine Sample #1 (HO), #2 (HP), #3 (MP) and #4
153 (LO). We combine the sample name with the applied capillary pressure (e.g., HO13.8 at
154 an imposed capillary pressure of 13.8 kPa) to denote an experiment. Water flow
155 experiments were conducted in these samples with frequent X-ray CT imaging to better
156 understand the dynamic invasion/drainage processes of CO_2-water and impacts of matrix
157 properties.

158 With an aim to quantify the surface wettability of each sample, we conducted contact
159 angle measurements of a water droplet on the sample surface at ambient conditions. The
160 measured air-water contact angles (i.e., 21 ± 2.6°, 22 ± 2.0°, 22 ± 0.7°and 46 ± 0.9° for
161 HO, HP, MP, and LO, respectively) indicate that the four samples are water wet (see
162 more details in Figure S2 of SI). The sandstone rocks (HO and HP) are composed mainly
163 of quartz (90%) and non-swelling kaolinite (7%), and we do not expect considerable
164 changes of pore geometry after sample exposure to deionized (DI) water. Sample MP is
165 composed of quartz (61%), feldspar (12%), montmorillonite (15%) and non-swelling
166 illite (12%). Although montmorillonite may potentially swell and reduce the matrix
167 porosity and permeability, its impacts on the CO_2-water flow in the fracture-matrix

system may not be pronounced due to the large contrast of capillary pressure-saturation characteristics between fracture and matrix. Also note that we measured the sample porosities, and characteristic curves (P_c-S relations) and conducted all of the water drainage experiments after fully saturating with DI water, thus the potential impacts from clay swelling have been compensated for. Sample LO is composed of calcite (70%), dolomite (20%), anhydrite (4%), and clay (0.3%), thus the impacts from exposure to DI water were expected to be very small (see more details on the sample mineralogy in Table S1 and S2 of SI).

2.2 Experimental setup and procedures

Figure 2b presents a schematic of the experimental setup, consisting of a reaction vessel and a pressure system that allows for CO_2 and water flow limited to a gauge pressure of 1035 kPa. Rocks were cored and end faces were sawn flat and sanded as smooth as necessary to fit into the acrylic core holder with an inner diameter of 5.08 cm and a length of 14 cm. The core samples were maintained dry in an oven at 60 °C prior to use. The rock core was then pressed against a filter paper disk in contact with the capillary ceramic plate. This arrangement was stabilized by a stiff spring at the top of the custom core holder. Two different types of ceramic plates (Soilmoisture Equipment Corp., CA) were used for Samples HO and HP and Samples MP and LO. Ceramics I and II have a porosity of 0.45 and 0.34, a water absolute permeability of 6.0 and 0.17 mD, and a capillary entry pressure of 100 and 300 kPa, respectively (see Table 1). The space between the vessel walls and the rock represents vertical fractures surrounding the matrix. A single sheet of filter paper disk (Glass microfiber filter GF/D, Whatman) between the core bottom and the ceramic plate was used to simulate a horizontal fracture

between the matrix blocks, similar to Stone et al. (1992). The fracture thickness and porosity are 0.8 mm and 0.6, respectively, while the fracture capillary pressure vs. water

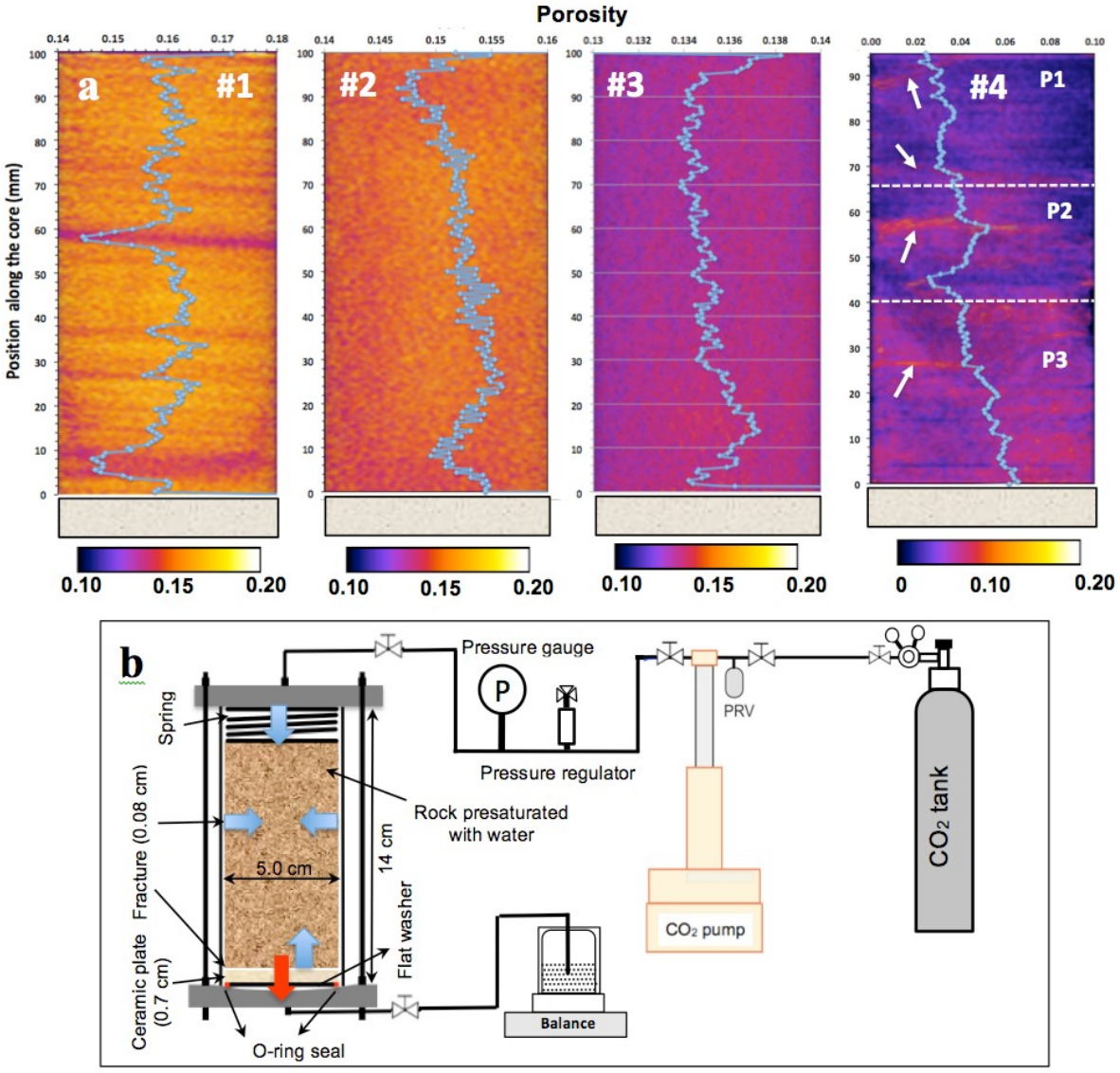

saturation relations were measured and the dynamic CO_2 invasion into the top matrix block was monitored through frequent X-ray CT scans (see Section 2.3).

Figure 2. (a) 2-D porosity maps derived using X-ray CT scans and profiles (blue lines) of slice-average porosity for the four core samples. Brighter color indicates higher porosity as depicted by the color bar. The white dotted lines for #4 in (a) marked the

198 boundary of the three portions indicated by the porosity distribution from the X-ray CT
199 image. The white arrows indicate the natural fractures in each portion. (b) Schematic of
200 the experimental setup that allows for CO_2 invasion (blue arrows) from the horizontal
201 fracture and from the vessel open space (representing fractures) next to the top and side
202 of the core sample, and for downward water drainage (red arrow) through the horizontal
203 fracture.
204
205 Before each experiment, the oven-dried rock core, filter paper, and ceramic plate were
206 first stacked and CT-scanned in the reaction vessel. The vessel was connected to vacuum
207 at -101 kPa for over 2 hours, followed by DI water injection through the bottom valve
208 until the sample core was completely submerged in water. The bottom valve was then
209 closed, and vacuum was maintained for 1-3 days depending on the samples used. After
210 saturating with water, the ceramic plate established a threshold pressure for CO_2 invasion,
211 below which the plate will be fully saturated with water. During the tests, the pressure
212 difference between CO_2 and water (at atmospheric pressure) was controlled and
213 maintained higher than the capillary entry pressure of the rock core, while lower than the
214 value of the ceramic plate. In this way, the bottom ceramic plate was maintained fully
215 water saturated (verified by CT images) at room pressure. Thus only downward drainage
216 of water from the stacked column to the outlet through the bottom ceramic (marked by
217 the red arrow in Figure 2b) is expected.
218 During each experiment, water between the rock core and vessel drained first,
219 allowing for CO_2 invasion at the top and from the circumferential surfaces of the rock
220 core. Water desaturation in the horizontal fracture could also occur, depending on the

applied gauge pressures of CO_2 and capillary entry pressure of the fracture. Water was drained through the ceramic plate and the outflow tube into an outflow reservoir containing DI water at the bottom. The water outflow mass was monitored by weighing the outflow reservoir on a balance. CO_2 was supplied to the vessel via a precise pressure regulator (Parker Hannifin Corp., US) at a resolution of 1.4 kPa from a 500D ISCO pump (Teledyne ISCO, NE) operated in a constant pressure mode. The setup allows frequent X-ray CT scans without disconnecting the reaction vessel from the pressure and drainage lines. The vessel containing the core sample was oriented vertically to investigate potential gravity effects, and positioned horizontally for very brief (when compared to the time needed for drainage) durations when an X-ray CT scan was conducted. A GE LightSpeed 16 CT Scanner was used to visualize the 3-D CO_2 distribution, and image data were used to calculate CO_2 saturation at a voxel size of 0.1925×0.1925×0.625 mm^3. Scans in each experiment were performed at 120 kV and 160 mA. Each CT scan took 24s, which is short in relative to the time scale of fluid migration in the rock samples.

The sample porosity (ϕ) and CO_2 saturation (S_{CO_2}) in the rock core and the horizontal fracture during each test were obtained from background and experimental scans, as given in the followings:

$$\phi = \frac{CT_{watersat} - CT_{dry}}{CT_{water} - CT_{air}} \tag{1}$$

$$S_{CO_2} = \frac{CT_{watersat} - CT_{\exp}}{CT_{watersat} - CT_{dry}} \tag{2}$$

where CT is the CT number in Hounsfield units computed for each voxel and that includes contributions from each pure component material present in the system (i.e., air, DI water, CO_2, and rock). The $CT_{watersat}$ and CT_{dry} refer to the CT values for each voxel of

243 water-saturated and oven-dried core, while $CT_{\exp}$ is the CT value obtained at different
244 times during each CO_2 displacement experiment. The CT numbers of the two pure
245 reference fluids, water (CT_{water}= 0) and air (CT_{air}= −998) are known from previous
246 calibration. Note that the two equations are derived originally from the linear attenuation
247 coefficients,μ (the truly measurable quantity by X-ray absorption), and uses CT
248 $\infty (\mu - \mu_{water})/\mu_{water}$ (Akin and Kovscek, 2003). They also imply that the CT number of a
249 voxel can be expressed as the linear combination of the CT numbers associated with the
250 volume fractions of each of its components. This assumption is justified by the linear
251 attenuation coefficient (thus the CT number) is proportional to the bulk density of
252 materials for X-ray energies above 100 keV (Wellington and Vinegar, 1987; Peters and
253 Hardham, 1990; Pini and Madonna, 2016). In Eq. (2), the CT numbers of air-saturated
254 and CO_2-saturated core are assumed be equal since the similar density of CO_2 and air at
255 the low imposed pressures in this study.

256 Applying equations (1) and (2) to each voxel, X-ray CT images have been widely
257 used during core-flood experiments to better understand the CO_2-water flow and
258 displacement characteristics at the core- and sub-core scales (Perrin and Benson, 2009;
259 Shi et al., 2011; Krevor et al., 2012; Berg et al., 2013; Zhang et al., 2014; Xu et al.,
260 2020). In this study, slice-averaged properties were calculated using CT numbers
261 averaged over a circular cross section (slice). The core porosity determined from X-ray
262 CT scans was comparable to that calculated gravimetrically from core mass changes at
263 dried and saturated conditions.

2.3 Gas intrusion capillary pressures of matrix cores and fracture

We cut thin disks (5.0 cm diameter and 1.0 cm thickness) from core samples of each rock described above, and measured their gas intrusion capillary pressures using the pressure plate method (Dane and Hopmans, 2002; Tokunaga et al., 2017). A 1500 kPa chamber (Soilmoisture Equipment Corp., US) was used, and compressed nitrogen was supplied to the chamber via a two-stage pressure regulator. The outflow tube from the pressure plate led into the bottom of an outflow reservoir containing DI water, and the free surface of this reservoir was kept at the same level as the plate. This method is well-suited for directly controlling P_c via changing pressure differences above a porous ceramic plate. We assume no considerable impact of gases (CO_2 or N_2) on P_c-S measurements because of the similar interfacial tensions for CO_2-water (71.03 mN/m at 100 kPa, 25 °C) and N_2-water (71-72 mN/m at <12 MPa, 25-30 °C) at the experimental pressure and temperature conditions (Massoudi and King, 1974, Chun and Wilkinson, 1995). The sample disks were initially saturated with DI water, and the applied P_c and corresponding water saturations in the disks were monitored using a precise pressure gauge and by frequently weighing the disks. The equilibrium water saturation in a sample for a particular P_c was then determined at constant mass. Figures 3a and 3b display the P_c-S_w functions for Samples HO, HP and MP, with error bars obtained from multiple sample disks. For Sample LO, two thin disks were obtained from the rock plug at locations next to P1 and P3, while sampling from P2 was difficult due to the open fracture.

Figure 3c shows the very different P_c-S_w functions for P1 and P3 induced by potential micro-fractures within the centimeter scale core sample. Mirzaei and Das (2007) performed a comprehensive modeling sensitivity analysis on the micro-heterogeneity

effects on P_c-S_w functions, and conduced a non-linear correlation between them, depending highly on the distribution of micro-heterogeneity. For larger scale fracture-matrix systems, the CO_2-water flow and CO_2 storage efficiency would be collectively affected capillary and gravity forces (Ide et al., 2007). In these systems, impacts from fracture orientation, connectivity, and transmissibility relative to the matrix will be more pronounced.

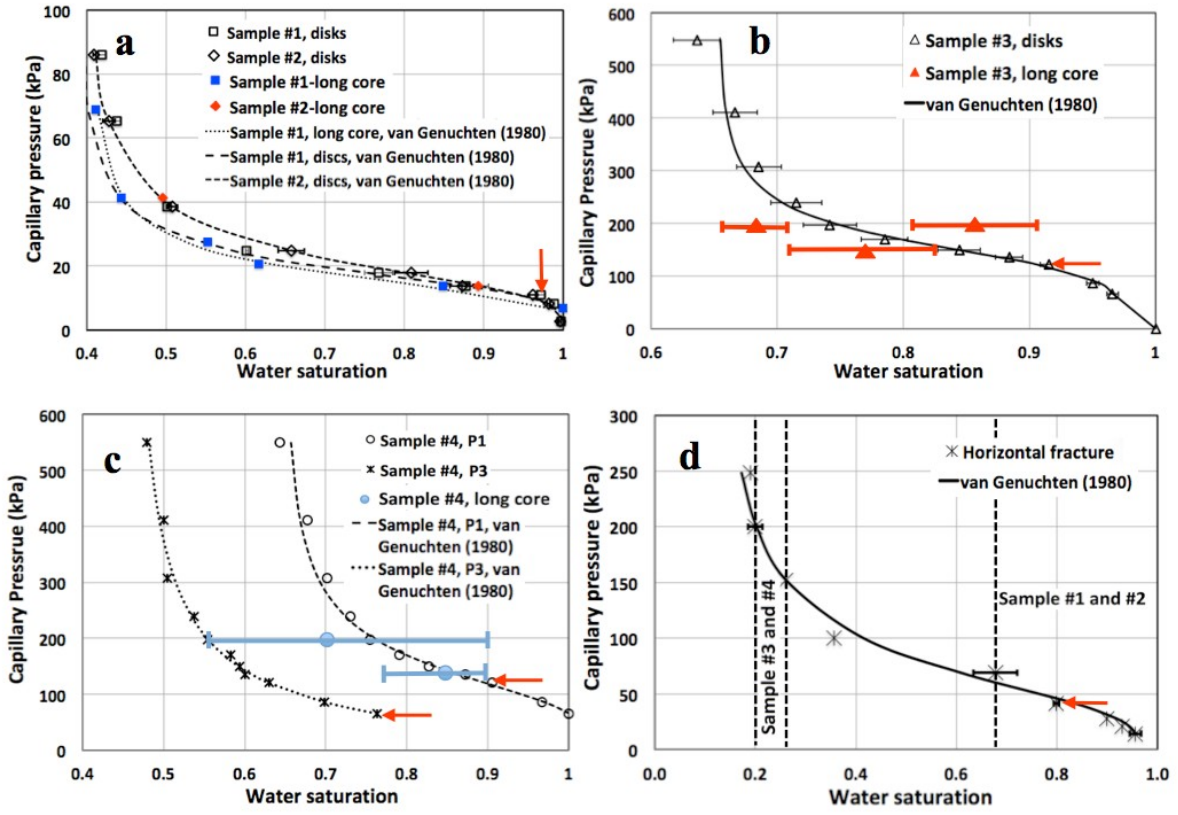

Figure 3. Measurements of the P_c-S_w functions for (a) Samples #1 (HO) and #2 (HP), (b) Sample #3 (MP), and (c) Sample #4 (LO) using 1.0 cm thick disks (black symbols) and 9.5-10 cm long whole core samples (color symbols). The error bars (black) in (a) and (b) were obtained from multiple disk measurements. P1 and P3 in (c) denote the top and bottom portions of Sample LO shown in Figure 1. (d) Measurements of the P_c-S

functions for the horizontal fracture, with the error bars obtained from two repeated tests. The colored bars in (b) and (c) indicate the range of water saturations in the long core samples measured from water drainage tests. The dashed lines in (d) bound the range of fracture water saturations during the water drainage experiments in the different rock samples. The red arrows indicate the capillary entry pressure measured for core samples and the bottom fracture.

The P_c-S_w function of the horizontal fracture in the stacked columns was quantified through water drainage tests. The fracture water saturations ($S_{w,f}$) under different applied P_c were determined through X-ray CT images. Figure 3d displays the P_c -$S_{w,f}$ relation, with error bars obtained from two repeated tests at 13.8, 68.9 and 200 kPa.

The capillary pressure characteristics of both matrix cores and the horizontal fracture can be described by the van Geuchten (1980) model as follows:

$$P_c = \frac{1}{\alpha}\left[\left(\frac{S_w - S_{w,r}}{1 - S_{w,r}}\right)^{\frac{-1}{m}} - 1\right]^{1-m} \quad (3)$$

where $S_{w,r}$ refers to the residual water saturation, and α and m are fitting parameters. Table S3 of the SI lists the fitting parameters of the van Genuchten (1980) model, with R^2 values higher than 0.99. The capillary entry pressure refers to the minimum P_c required for CO_2 intrusion into the water-saturated core sample or fracture, which corresponds to the inflection point identified by the red arrows in the P_c-S_w relations in Figure 3. The values for Samples HO, HP and MP are measured as 13.8, 13.8, 135 kPa. The pore size interpreted from the capillary entry pressures ranges from 1-10 μm, which are consistent with the sandstone classifications from Nelson (2009). For Sample LO, the capillary entry pressures are 135 and 66 kPa for P1 and P3, respectively, while the value for the

321 horizontal fracture is 41.4 kPa. In the stacked column tests at P_c > 68.9 kPa, we expect
322 considerable fracture desaturation and concomitant reduction of capillary continuity
323 between the top and bottom matrix blocks (See Section 3.2).

324 The non-zero, non-constant, and porous-medium-like capillary pressure of the
325 horizontal fracture in this study is representative of certain types of natural fractures, due
326 to (1) the large variations of fracture apertures, (2) the complex geometry of a fracture
327 network, and (3) the wide presence of mineralization in fractures. Ramsay (1980)
328 reported the observations of tectonically deformed crustal rocks and cracks and fissures
329 filled with silicate or carbonate mineral. The open microfractures filled with crystalline
330 material derived from pressure solution in the rock matrix and chemical transfer of this
331 material into the low-pressure fluid-filled space, a mechanism termed 'crack-seal'.
332 Morrow et al. (1990) further reported the permeability measurements of the mineral-filled
333 fractures in the Mesaverde formation rock samples, which were of the same order as the
334 surrounding matrix and presented water-saturation dependent behavior, similar to the
335 porous matrix. Parry (1998) presented the fault-fluid compositions and solubilities of the
336 fracture-sealing minerals, while Fletcher and Merino (2001) summarized the published
337 insights into the mineralization and crystal growth in rock fractures, and proposed models
338 on the coupling between mineral growth kinetics and mechanical response of the rock. In
339 summary, the wide presence of mineralization in natural fractures and the resulting
340 changes in fracture properties (e.g., permeability, capillary pressure and chemistry)
341 impose fracture P_c-S_w functions similar to porous media, resulting in a large range of
342 contrast with matrix. The CO_2-water flow fundamentals in these fractured porous media
343 are of importance to GCS and other subsurface processes.

344 Also note the capillary entry pressure of the fracture in the stacked columns is higher
345 than that of the matrix in Samples HO and HP. This may reduce the effect of the water-
346 flow barrier of the fracture and help highlight the importance of capillary continuity. The
347 experiments still allow us to focus on CO_2-water displacements in these fracture-matrix
348 systems.

349 **2.4 Water Drainage Experiments**

350 Twelve water drainage experiments were conducted to investigate the CO_2-water
351 displacements with controlled P_c up to 200 kPa (see Table 2). Five tests in the column
352 stacked with Samples HO (HO13.8, HO30.7, HO27.6, HO41.4 and HO68.9) were
353 conducted to investigate the fundamentals of CO_2-water flow and CO_2 saturation in
354 matrix with high fracture water saturation, thus high capillary continuity. Tests under
355 varying imposed capillary pressures (from 13.8 to 68.9 kPa) were used to understand the
356 impacts of capillary pressures.

357 Two different comparison and sensitivity analyses were conduced. The first analysis
358 focused on the effects of bedding orientation by two experiments with Sample HP
359 (HP13.8 and HP41.4) maintaining similarly high capillary continuities in fracture. For the
360 second sensitivity analysis, experiments were conduced targeting at water drainage across
361 the single desaturated fracture (thus reduced capillary continuity) in Sample MP (MP150,
362 MP200a, MP200b), as well as water drainage across multiple desaturated fractures in
363 Sample LO (LO150, LO200).

364 During the experiment, the impacts of CO_2 dissolution and mass transfer is expected
365 to be minimal, because of (1) the low CO_2 solubility in water (0.068 mol/L, from Zhao et
366 al., 2015) under the low pressure ($\leq$ 200 kPa) and temperature (25 °C) conditions in this

study, and (2) the very small impacts of CO_2 dissolution and mass transfer on two-phase displacement and distribution under drainage conditions. For instance, in a previous study (Chang et al., 2017), we investigated supercritical CO_2 ($scCO_2$)-water displacement and dissolution in an mm-scale micromodel at 9 MPa and 40 °C, and monitored the CO_2 dissolution and mass transfer into residual water. Results showed overall constant CO_2 saturation after drainage and stable two-phase distribution in the micromodel due to the continuous inflow of CO_2, although CO_2 dissolution occurred at the two-phase interface is considerably higher (1.225 mol/L) at the elevated pressure and temperature.

3. Results

3.1 CO_2-water flow in the matrix with high fracture water saturation

Five drainage experiments were conducted in Sample HO at varying P_c from 13.8 to 68.9 kPa. During each experiment, dynamic CO_2 invasion and water drainage were monitored by frequent X-ray CT scans and the images were used to calculate both slice- and core-average CO_2/water saturations at a number of times until a capillary quasi-equilibrium was reached. According to the P_c-$S_{w,f}$ characteristics of the fracture in Figure 3d, fracture water desaturation to 0.68-0.96 is expected, depending on the imposed P_c values.

3.1.1 Dynamic water drainage and CO_2 saturation

Figure 4a shows selected time-lapse images of 3-D CO_2 distribution (purple color) in test HO13.8. The numbers in the parentheses are experimental time and core-average CO_2 saturations, respectively. Also displayed in the figure (the last sub-image) is the 3-D porosity distribution for comparison. The temporal CO_2 distributions indicate preferential

389 CO_2 uptake along multiple high-porosity layers in contact with the circumferential
390 surface. The variations of the slice-averaged CO_2 saturation along the core sample from
391 top to bottom shown in Figure 4b are overall consistent with those of porosity (not in a
392 perfect correlation however, indicating porosity and pore size are not necessarily
393 correlated). The inconsistencies in correlation and offset of the peak CO_2 saturation vs.
394 porosity at some portions of the sample (e.g., marked by the red dotted lines at 50 mm, 70
395 mm and 78 mm from the sample top in Figure 4b) could be attributed to the competition
396 between different CO_2 fingers from the circumferential surface. As shown in Figure 4a,
397 CO_2 fingers developed preferentially along the high porosity layer at 38 mm, which
398 induced drainage of resident water towards the core bottom and resulted in the other CO_2
399 fingers to develop slightly beneath the peak porosity positions at 50 mm, 70 mm and 78
400 mm. At the bottom portion of the core (e.g., at 90 mm and close to the outlet), the
401 variations of CO_2 saturation are more consistent with those of porosity as water drainage
402 pathway was shortest and easiest towards the outlet. The core-average CO_2 saturation
403 increased with time for 78 hours, and remained relatively constant at 0.15 ±0.006 after
404 exposure to CO_2 until 288 hours, when the experiment was stopped.

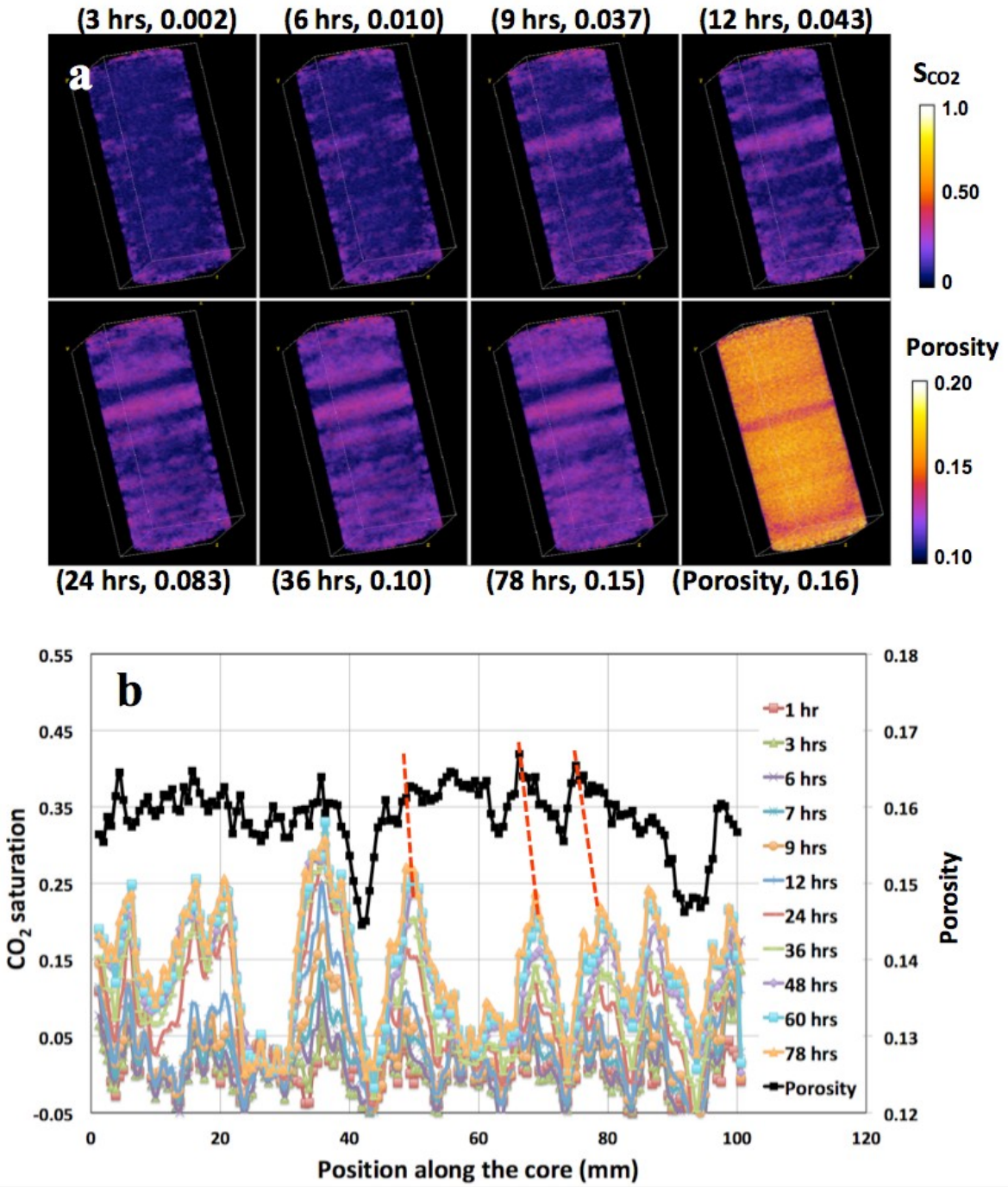

405 **Figure 4.** (a) Images of 3-D CO_2 saturation from core top to bottom acquired during the
406 water drainage experiment in Sample HO at P_c=13.8 kPa, as well as the 3-D porosity
407 distribution in the last sub-image. Brighter color indicates higher CO_2 saturation and
408 porosity as depicted by the color bar. (b) Slice-averaged porosity and CO_2 saturations

409 change with time. The numbers in the parenthesis in (a) denote exposure time and core-
410 average CO_2 saturation or the core-average porosity. Water saturation in the bottom
411 fracture maintained high at 0.96 during the experiment. The red dotted lines in (b) mark
412 the offset of the peak CO_2 saturation vs. porosity.

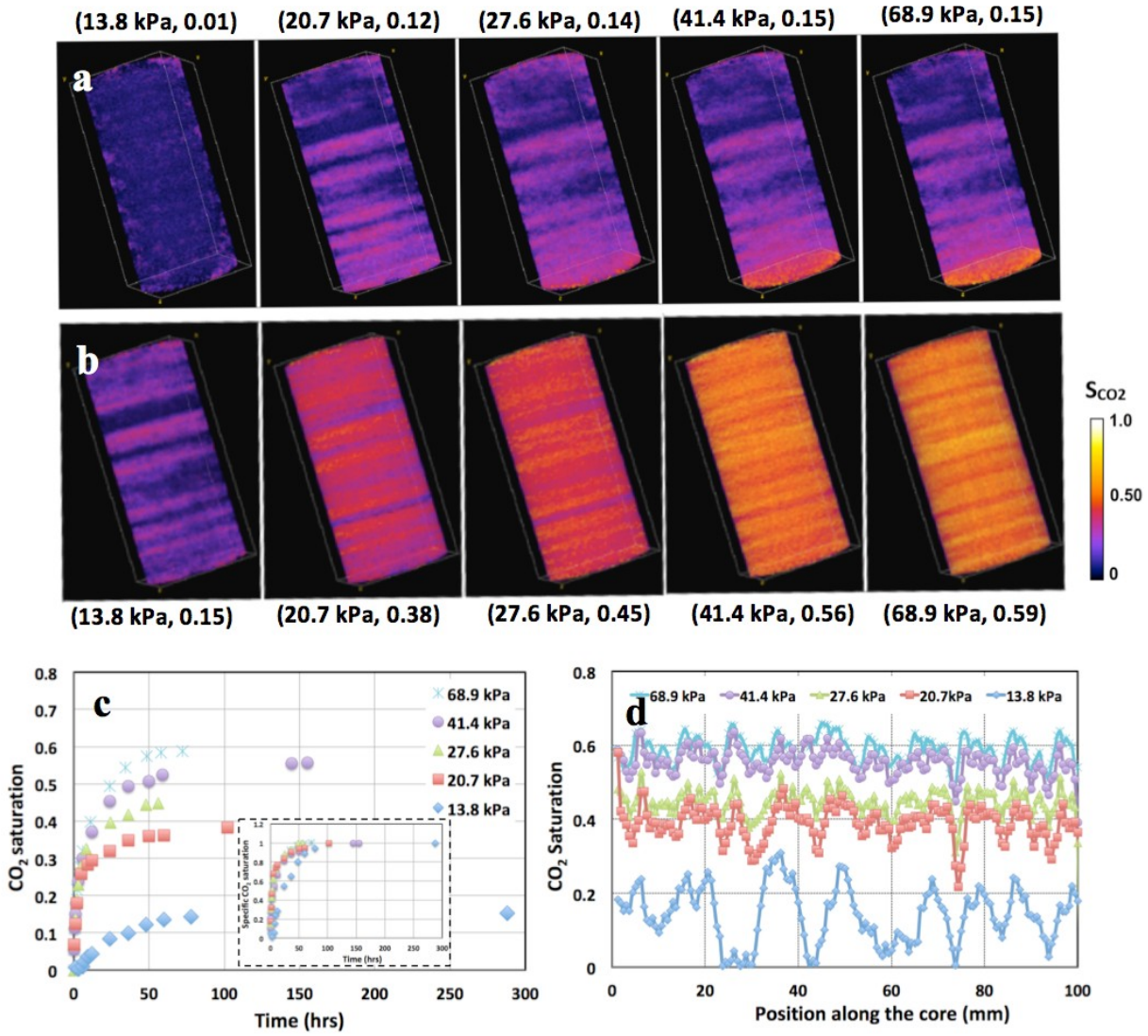

413 **Figure 5.** Images of 3-D CO_2 saturation from core top to bottom at (a) early time (1 hour)
414 and (b) the quasi-equilibrium state during drainage experiments in Sample HO at P_c-
415 =13.8, 20.7, 27.6, 41.4 and 68.9 kPa. The numbers in each parenthesis denote applied P_c

and core-average CO_2 saturation. (c) Core-average CO_2 saturation vs. exposure time acquired at different P_c, and (d) CO_2 saturation variations along the core from the top at quasi-equilibrium state for different cases. The inserted sub-image in Figure 5c presents the temporal changes of specific CO_2 saturation, the ratio between temporal CO_2 saturation and CO_2 saturation at capillary equilibrium, under different imposed capillary pressures. Note water saturation in the bottom fracture decreased from 0.96 to 0.68 with increasing capillary pressures during these experiments.

3.1.2 Effects of capillary pressure

The P_c effects on CO_2-water displacement in Sample HO were investigated by specifying CO_2 pressures of 20.7, 27.6, 41.4 and 68.9 kPa, while keeping water drainage pressure at atmospheric. X-ray CT images were obtained during each experiment until the CO_2 distribution and saturation in the core were stable with time. Figures 5 shows the CO_2 distributions at early time (Figure 5a, 1 hour) and quasi-equilibrium state (Figure 5b) under the five capillary pressures. When P_c was increased above the capillary entry pressure of the core (13.8 kPa), most CO_2 invaded into the rock along its circumferential surface, preferentially through the higher porosity layers (again, not perfectly correlated). This dominant circumferential inflow of CO_2 from the surrounding fractures can be attributed to the larger circumferential area compared to that of the top surface and reduced water drainage pathway towards the bottom fracture than axial flow from top. For instance, we observed high CO_2 saturations in the bottom portion of the core at 1 hour, where the water drainage pathway was shortest towards the outlet. Figures 5c and

5d depict the core-average CO_2 saturations vs. time and variations of slice-average values along the core at the quasi-equilibrium state for each case. We may infer that the core-scale CO_2 saturations increase with increasing P_c with more CO_2 uptake in the low-porosity layers, smoothing the CO_2 saturation variations along the core sample. We also define a specific CO_2 saturation, the ratio between temporal CO_2 saturation vs. CO_2 saturation at capillary equilibrium, and present the temporal changes of the value in the inserted sub-image in Figure 5c. As the imposed capillary pressures are higher than the capillary entry pressure (P_c>13.8 kPa), the temporal increases in the specific CO_2 saturation follow the similar trend and time scale to converge at the capillary equilibrium saturation, as the dominant CO_2 invasion from the circumferential surface and water drainage in the normal direction. This is different from 1-D two-phase flow, where confining pressure is applied and CO_2-water flow is prohibited across the circumferential surface. The quasi-equilibrium P_c vs. water saturation generally follows the P_c-S_w curve obtained from disk measurements in Figure 3a.

3.2 Effects of bedding orientation

Two flow experiments (HP13.8 and HP41.4) were conducted in Sample HP to better understand the impacts of matrix bedding orientations on CO_2-water displacement. Sample HP was cut parallel to the bedding with porosity variations from 0.15 to 0.16 along the long axis. During these experiments, high water saturations (>0.60) were maintained in the horizontal fracture (Table 2), resulting in high capillary continuity for water drainage across the fracture.

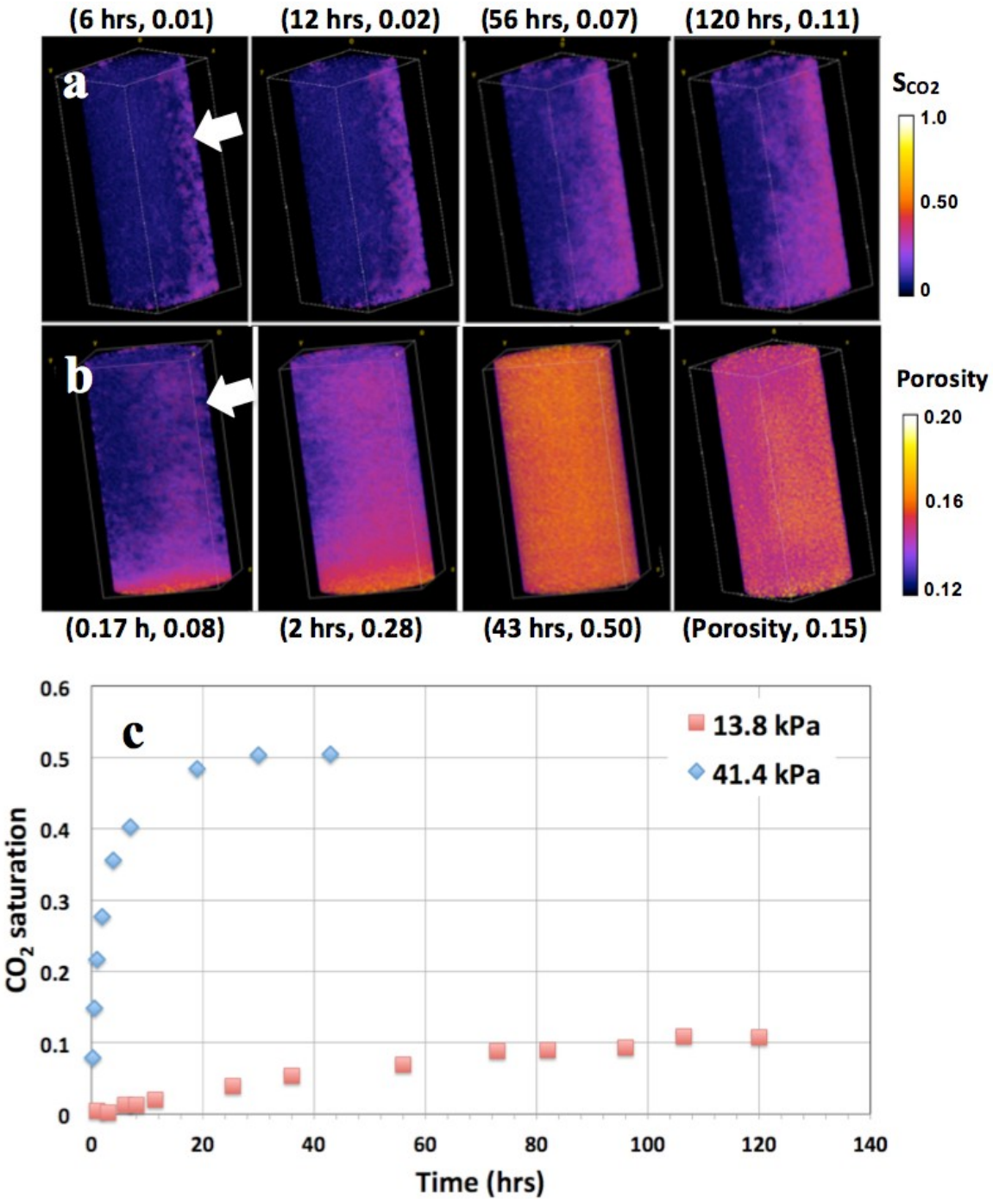

Figure 6. Images of 3-D CO_2 saturation from core top to bottom during the water drainage experiments in Sample HP at (a) P_c=13.8 kPa and (b) 41.4 kPa, as well as the 3-

D porosity distribution in the last sub-image. (c) Core-average CO_2 saturation vs. exposure time at different P_c. The numbers in each parenthesis denote the exposure time and core-average CO_2 saturation or the core-average porosity, while the white arrows show the direction of CO_2 invasion. Water saturation in the bottom fracture is 0.96 and 0.80, respectively, in (a) and (b).

Figures 6a and 6b present the dynamic CO_2 saturations and distributions in Sample HP during the two experiments. In both cases, CO_2 preferentially invaded the core sample from one side (high porosity), and displaced resident water toward the opposite side (low porosity), where the displaced water migrated downward under single-phase water flow condition during most of the experiment duration. The core-average CO_2 saturation was stable at 0.11 after 120 hours in HP13.8 and 0.50 after 43 hours in HP41.4 (see Figure 6c). These quasi-equilibrium CO_2 saturations are close to those (0.15 and 0.56) obtained in Sample HO at the same P_c values as should be expected. The parallel bedding in Sample HP, however, facilitated downward drainage of water, and greatly shortened the time scale to reach equilibrium compared to that in Sample HO at the same P_c=41.4 kPa (see Table 2).

3.3 Water drainage across single desaturated fracture and fracture-matrix interactions

CO_2-water displacements after fracture desaturation were investigated in the column stacked with Sample MP, with a higher capillary entry pressure (135 kPa) relative to the horizontal fracture (69 kPa). For the two experiments (MP150 and MP200a), we expected (1) larger water desaturation in the fracture than that in the matrix (see Figure 3b and d),

and (2) considerable reduction in the capillary continuity of the fracture with increased water drainage resistance, due to the blockage of water flow (thus decrease of water relative permeability) across the bottom fracture by invaded CO_2.

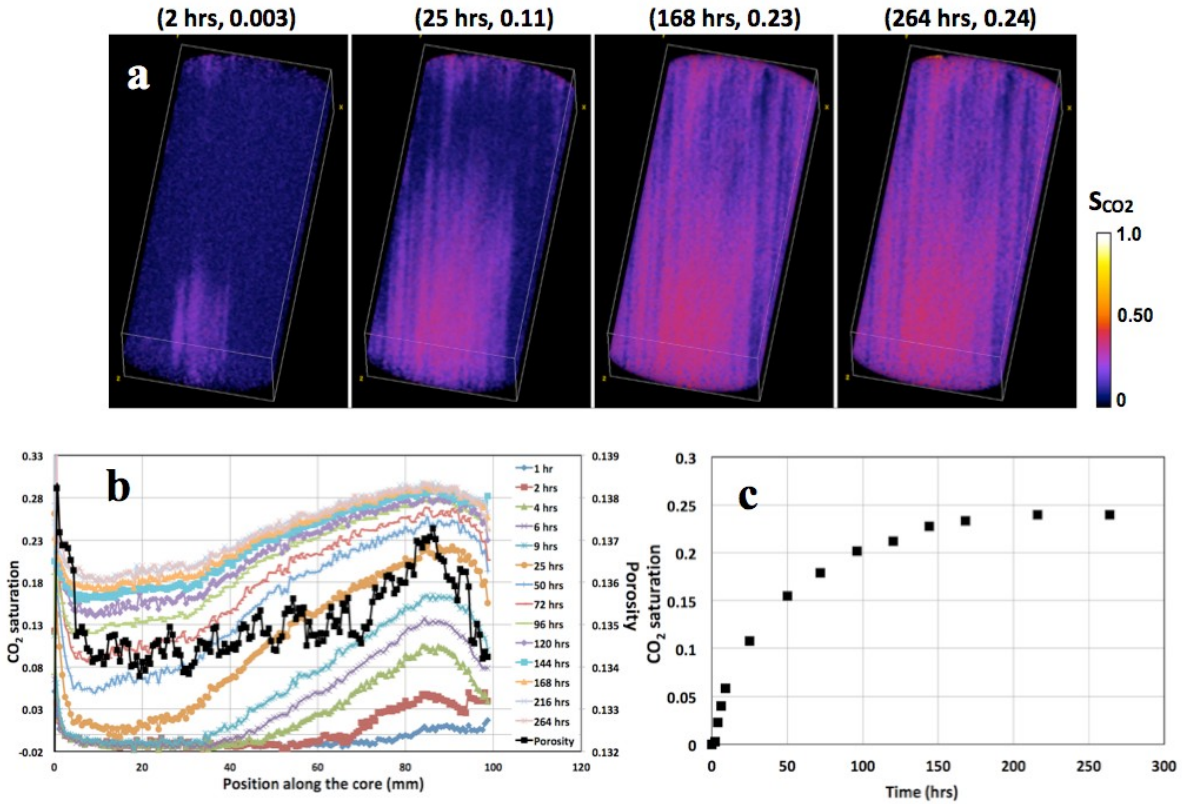

Figure 7. (a) Images of 3-D CO_2 saturation from core top to bottom during the water drainage experiment in Sample MP at P_c=150 kPa (MP150), (b) slice-averaged variations of porosity and CO_2 saturation along the core from the top at different exposure times, and (c) core-average CO_2 saturation vs. exposure time. Water saturation in the bottom fracture is 0.50 during the experiment. The numbers in the parentheses in (a) denote the exposure time and core-average CO_2 saturation.

Figures 7a and 7b show the selected images of CO_2 distribution and CO_2 saturation along the core at different times for MP150. It can be seen that CO_2 initially invades the higher porosity portion of the core at the bottom close to the horizontal fracture and propagates upwards in the matrix. This process may retard CO_2 invasion from the circumferential surface. The core-average CO_2 saturation increases with time and stabilizes at 0.24 after 264 hours (Figure 7c). The pair of specified P_c and measured core-scale CO_2 saturation follows the P_c-S curve measured from 1 cm thin disks in Figure 2b. The slice-average CO_2 saturation shown in Figure 7b, however, varies greatly from the top (0.18) to the bottom (0.30), indicating the impact of sub-core scale heterogeneity in the 10 cm long core. By the end of the experiment, water saturation in the bottom fracture is 0.50, considerably higher than the value of 0.26 measured for the fracture P_c–$S_{w,f}$ function in Figure 3d. Also note the pronounced difference in equilibrium matrix CO_2 saturation between Samples HO and HP vs. Sample MP. At similar porosities and when maintaining sufficient fracture water saturation ($\geq$ 0.5), the maximum storage capacity in Samples HO and HP (0.60 at 68.9 kPa) could be as much as 2.5 times higher than that in Sample MP (0.24 at 150 kPa).

The unexpectedly high fracture water saturation in MP150 can be attributed to the countercurrent flow of CO_2 and water across the fracture-matrix interface, i.e., CO_2 invades the matrix core from the bottom fracture and water drains from the matrix core across the same interface. To better understand the process, we compared the CO_2 distribution in the bottom portion of the core next to the horizontal fracture (Figures 8a and 8b), with the water distribution within the fracture (Figures 8c and 8d) at early time (1 hour) and the end of the experiment (264 hours). Once exposed to CO_2, the bottom

fracture is invaded by CO_2 and resident water is partially displaced, as indicated by the two black patches representing low fracture water saturations in Figure 8c. P_c in these patches may exceed the capillary entry pressure of the matrix core above, thus CO_2 invasion into the rock matrix is available. At the same time, drainage of water occurs downward next to the CO_2 flow pathway, resulting in a high water saturation patch in the bottom fracture in Figure 8c (see the bright band in the middle). Note the consistent geometry of the high $S_{w,f}$ patch vs. CO_2 plume in the bottom portion of the core. This high $S_{w,f}$ patch hydraulically bridges the top core and bottom ceramic plate, providing an efficient water drainage pathway across the fracture and allowing for continuous CO_2 invasion i ısion of CO_2 in t racture, resulting

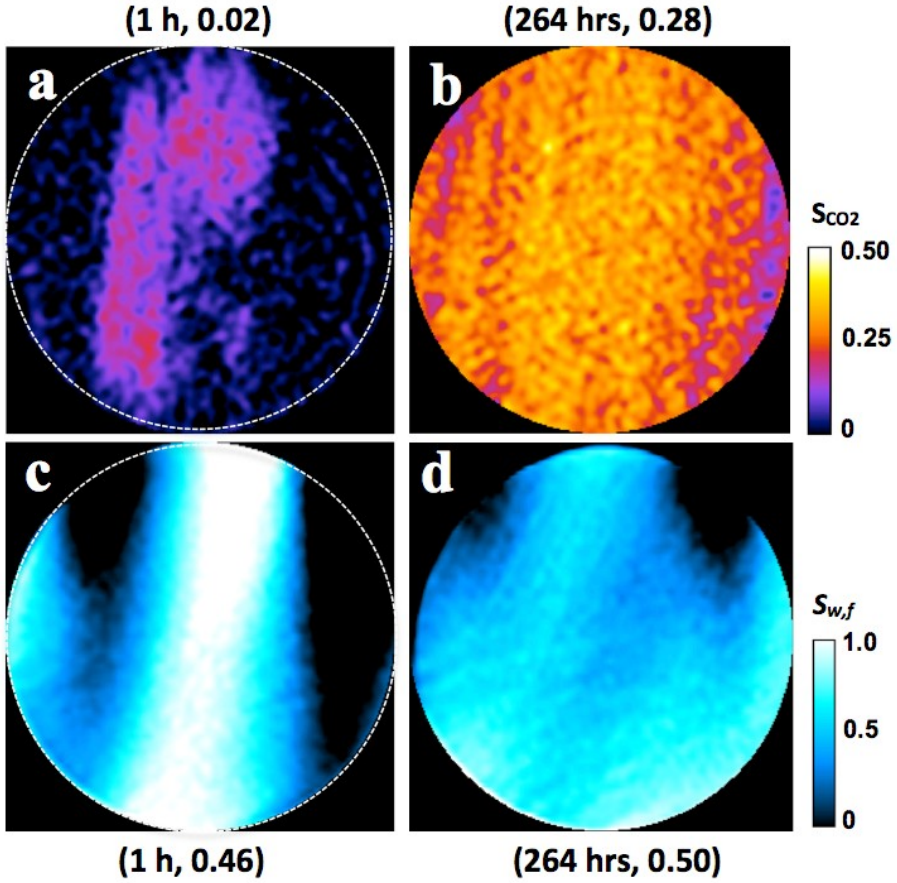

Figure 8. Images of 2-D average CO_2 saturation within the bottom portion (30 mm above the horizontal fracture) in Case MP150 at (a) early time and (b) quasi-equilibrium state, and images of 2-D fracture water saturation at (c) early time and (d) quasi-equilibrium

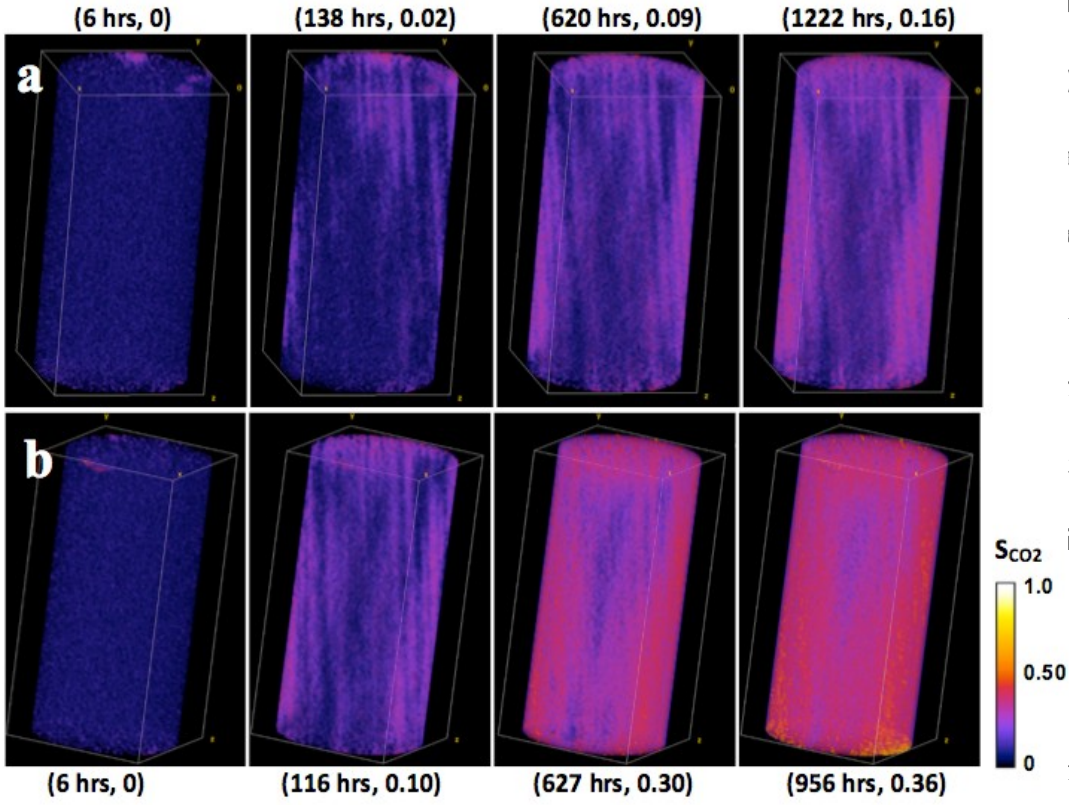

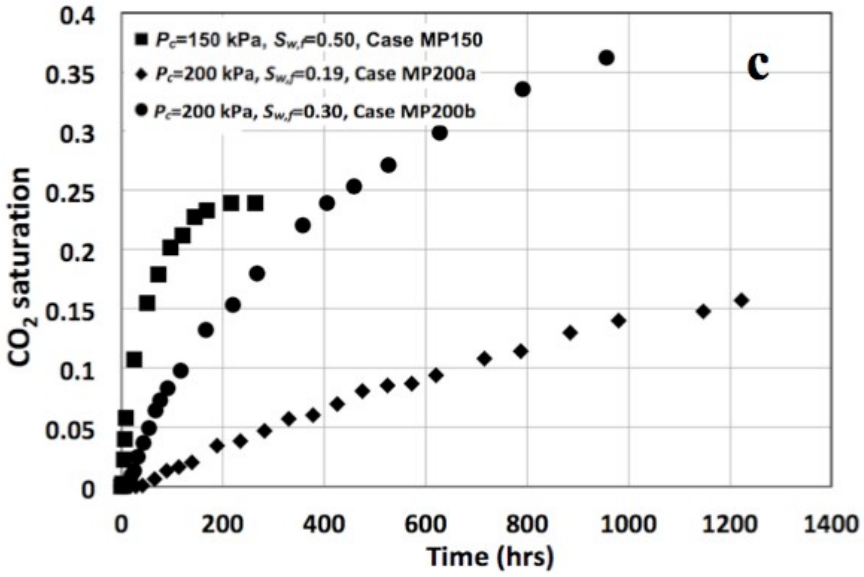

567 average CO_2 saturation increased slowly with time, and we stopped the test at 1222 hours
568 before reaching the capillary equilibrium. By the end of the experiment, the core-average
569 CO_2 saturation is 0.16, lower than the value in MP150 (0.24), although a higher P_c was
570 applied and maintained for a significant longer time (see Figure 9c). We then conducted
571 an additional drainage test (MP200b), in which the same P_c (200 kPa) was applied, while
572 the junctions between the surrounding and horizontal fractures were partially sealed by
573 epoxy coating around the circumferential surface of the horizontal fracture. The seal was
574 not perfect as a crack developed within the thin epoxy layer when pressed the core
575 against the ceramic plate, but was able to reduce CO_2 invasion and increase fracture water
576 saturation to 0.30. Figure 9b and 9c show the faster CO_2 invasion and higher CO_2
577 saturation in the core, when compared to Case MP200a under the same P_c. The three
578 drainage experiments indicate that efficient CO_2 uptake in the matrix and water drainage
579 across fracture are only possible when sufficient water saturation (thus capillary
580 continuity and water relative permeability) is maintained in the horizontal fracture. The
581 capillary continuity of the fracture can be greatly enhanced by fracture-matrix
582 interactions through a countercurrent flow between CO_2 and water, when (1) the P_c and
583 CO_2-water distribution are non-uniform in the fracture, and (2) the local P_c exceeds the
584 capillary entry pressure of matrix at the interface.

585 **3.4 CO_2-water drainage across multiple desaturated fractures**

586 We investigated the CO_2 uptake in the matrix and water drainage across a single
587 fracture from a number of cases (Samples HO, HP and MP). In this section, we present
588 CO_2-water drainage across multiple horizontal fractures from two experiments (LO150
589 and LO200) in the naturally fractured Duperow dolostone Sample LO. Sample LO is

590 characterized by three alternating fracture-matrix portions with capillary pressure
591 contrasts shown in Figure 3c.

592 Figures 10a and 10b show the temporal changes in core density (relative to the
593 initially water-saturated condition) after CO_2 exposure at P_c=150 and 200 kPa.
594 Calculating CO_2 saturations for each pixel Using Eq. (2) resulted in considerable noise
595 due to the low porosity nature of the core. Some pixels or portions of the sample were too
596 tight to have distinguishable CT signal changes between $CT_{watersat}$ and CT_{dry}, $CT_{watersat}$
597 and $CT_{\exp}$. Noise was further amplified as $CT_{watersat} - CT_{dry}$ (=0 or negative) was in the
598 denominator of Eq. (2). To reduce the noise, we converted $CT_{watersat}$ and $CT_{\exp}$ to density
599 $\rho_{watersat}$ and $\rho_{\exp}$ through a pre-established correlation function, and calculated density
600 changes ($\Delta\rho=\rho_{\exp}-$¿ $\rho_{watersat}$) to represent the CO_2 invasion and water drainage. In both
601 figures, brighter color refers to larger density reduction, thus higher CO_2 saturation. As
602 shown in Figures 10a and b, density reduction started in the four fractures at early time
603 (8.5 hours at P_c=150 kPa and 6 hours at 200 kPa), followed by matrix density reduction
604 until the end of experiments at 701 and 841 hours. A larger matrix density reduction was
605 also observed in the bottom portion of the core at later times (e.g., 262.5 hours in Figure
606 10a and 264 hours in Figure 10b). In Sample LO, the low matrix porosity and
607 permeability, and high capillary entry pressure hindered fracture-matrix interaction at the
608 interface. The fracture water saturations during the two experiments were measured at
609 0.26 and 0.21, following the fracture P_c-$S_{w,f}$ relation shown in Figure 3d.

610 We also calculated the slice-average CO_2 saturation using Eq. (2) by averaging the
611 $CT_{\exp}$, $CT_{watersat}$, CT_{dry} values over 50,000 voxels in each slice, and showed in Figure 10c
612 the variations along the core at the end of the two experiments. From the figure, we

observed (1) higher CO_2 saturations in the four fractures validating the initial assumption of drainage occurring first in the fractures (see the peaks marked by the black arrows), (2) the overall CO_2 saturation in P3 was higher than that in P1 and P2, and (3) CO_2 saturation in P3 increases with increasing P_c, while it remained constant in P1 and P2, independent of the P_c applied. At P_c =200 kPa, the average CO_2 saturation in P3 was stable at 0.44 after 841 hours exposure to CO_2, similar to the value of 0.45 obtained from thin disk P_c-S_w measurements (marked by the blue dashed line in Figure 10c). This indicated capillary equilibrium state in P3. The average CO_2 saturation in P1, however, remained low (0.10) by the end of the two experiments. Note the gas saturation measured from thin disks at the capillary equilibrium state is higher at 0.25 (marked by the blue dashed lines for P1 in Figure 10c). For water drainage from P1, the multiple desaturated fractures (including the two in P2, P3 and the one beneath the matrix) increased water flow resistance along the pathway, thus considerably reduced the drainage efficiency at the experimental time scale. At this point, the fractures served as barriers for further CO_2 invasion into matrix, similar to the modeling results from Bogdanov et al. (2003), who concluded that fractures can act as obstacles to the flow in their normal directions due to capillary effects. By the end of the experiments, the core-average CO_2 saturations were measured as 0.29 and 0.19 at P_c= 150 and 200 kPa (see Figure 10d).

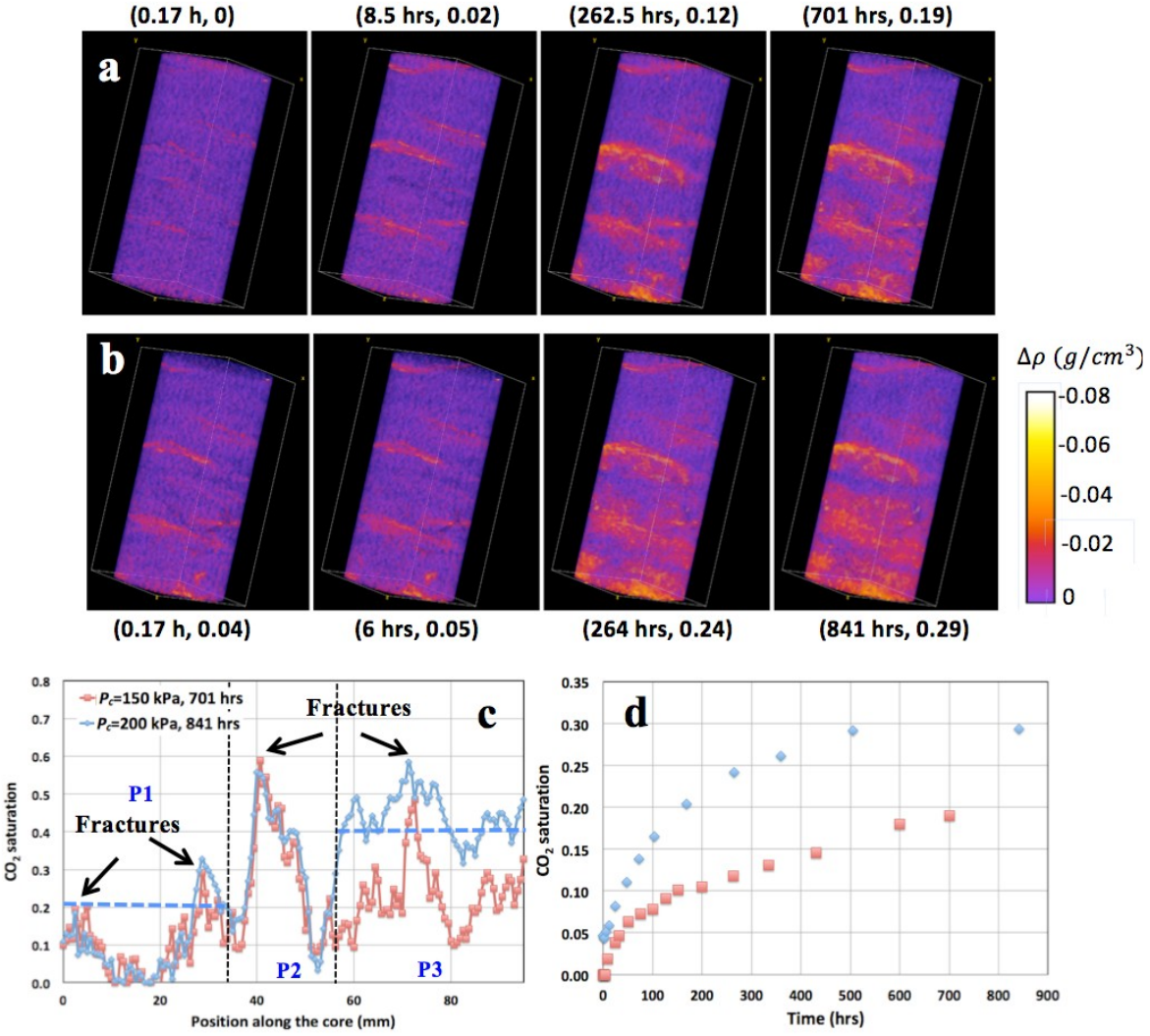

Figure 10. Images of 3-D density changes from core top to bottom in Sample LO during water drainage experiments at (a) P_c=150 kPa and (b) P_c=200 kPa. (c) Slice-average CO_2 saturation at the end of the two experiments, and (d) core-average CO_2 saturation vs. exposure time. The numbers in the parenthesis in (a) and (b) denote the exposure time and core-average CO_2 saturation. In (c), the black arrows mark the multiple peaks of CO_2

643 saturation in core fractures, the black dashed lines bound the three portions, while the
644 blue dashed lines indicate the average gas saturations in P1 and P3 from the P_c-S_w relation
645 measured with thin disks of Sample LO. Water saturation in the bottom fracture is 0.26
646 and 0.21, respectively in (a) and (b).

647 ## 4. Discussion

648 In Section 3.1 and 3.2, we investigated the CO_2-water flow in fracture-matrix systems
649 with high capillary continuity in the fracture. In Section 3.3 and 3.4, two different
650 comparison and sensitivity analyses were conducted with reduced capillary continuities
651 in the fracture and core samples having different properties. These experiments were
652 motivated by the long consideration of the assumption of the on-off fashion and constant
653 capillary entry pressure of natural fractures. The single-block concept has been widely
654 adopted for modeling multiphase flow in fractured reservoirs through the well-known
655 dual-porosity model (Warren and Root, 1963). In the model, the drainage of matrix
656 blocks by invading fluid occurs independently so that the performance of a stack of
657 blocks is equal to the performance of a single block multiplied by the number of
658 individual blocks. Theoretical analysis and examination of the field performance of some
659 fractured reservoirs, however, indicate the existence of some capillary continuity between
660 matrix blocks as (1) the existence of formation rocks that are not completely separated or
661 isolated from other blocks by open natural fractures (Festoy and van Golf-Racht, 1989;
662 Liu and Rutqvist, 2010), and (2) bridging of matrix blocks by residual water in fractures
663 that creates potential hydraulic connections for water drainage across the fractures (Sulak
664 1990; Hermansen et al. 1997; Agarwal et al. 1999; Rangel-German and Kovscek, 2006;

665 Rangel-German et al., 2006; Firoozabadi, 2000; De la Porte et al., 2005; Fernø et al.,
666 2011). Through a series of stacked-block experiments, Horie et al. (1990) and Stones et
667 al. (1992) reported that the fracture capillary pressure is water-saturation dependent, and
668 might have a functional form similar to that of a matrix. Reitsma and Kueper (1994)
669 measured the capillary pressure vs. saturation in a single, rough-walled fracture, which
670 was well represented by a Brooks-Corey porous media capillary pressure function with a
671 distinct entry pressure observed. The errors introduced when ignoring nonlinear k_r curves
672 and non-zero P_c in fractures were demonstrated by de la Porte et al. (2005), who
673 presented that displacement efficiency could be underestimated by a factor of two when
674 fracture capillary pressure was set to zero. A detailed investigation is required, which is
675 one of the objectives in this study, to better understand the impacts of the non-constant,
676 porous-like capillary pressure of fractures on CO_2-water drainage and CO_2 saturations in
677 fracture-matrix systems.

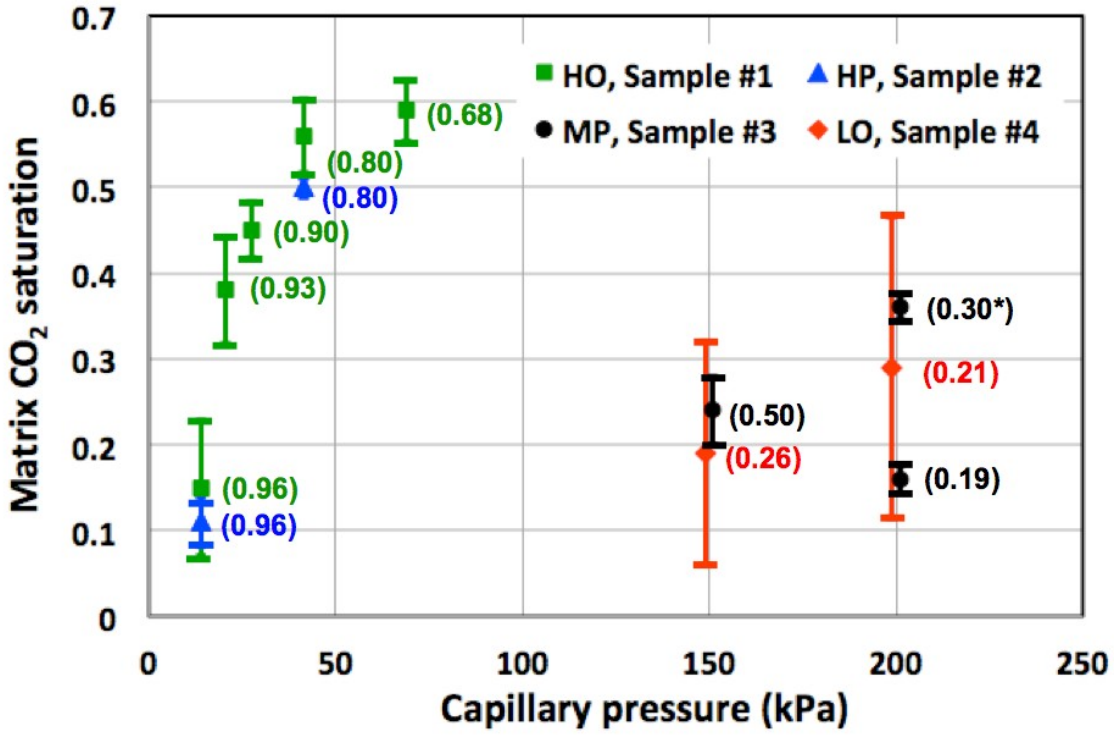

Figure 11. The relations between matrix CO_2 saturation vs. applied capillary pressure in the twelve water drainage experiments. The colored bars bound the standard deviations of CO_2 saturation along the matrix cores, calculated from each X-ray CT image slice at 0.625 mm thickness. The number in each parenthesis represents the fracture water saturation at steady state. *Note the fracture water saturation of 0.30 in MP200b was induced by reducing the peripheral area of fracture exposure to CO_2 through an epoxy sealing treatment.

Figure 11 summarizes the relationships of average matrix CO_2 saturation vs. applied capillary pressure in stacked fracture-matrix systems. The bars bound the standard deviations of CO_2 saturation along the matrix cores, calculated from each CT image slice (0.625 mm thickness). The numbers in parenthesis in the figure represent the

690 corresponding water saturations in the bottom fracture at steady state. Overall, there
691 exists a range of critical capillary pressure values below and above which the matrix CO_2
692 saturation vs. capillary pressure relations are considerably different. Here, when P_c is low
693 (<100 kPa) and fracture water saturations are high (>0.6), the matrix CO_2 saturations in
694 Samples HO and HP increase with increasing P_c, depending on the matrix P_c-S_w
695 characteristics. Note the matrix CO_2 saturations vary by a larger span in Sample HO
696 (indicated by the bars), where the bedding layers are normal to the water drainage
697 direction. Also recall the faster water drainage to the capillary quasi-equilibrium state (43
698 hours) in Sample HP at P_c= 41.4 kPa where bedding is parallel to the water drainage
699 pathway, compared to 145 hours required for Sample HO (Table 2). In Sample HP, CO_2
700 and water maintain high saturation along their individual pathways (see Figure 6) and
701 thus high relative permeabilities for both fluids. With frequent CT imaging, we directly
702 visualized the 3-D CO_2-water drainage in the stacked columns, and indicated the impacts
703 of matrix bedding orientations relative to the fracture that maintains high capillary
704 continuity (e.g., 0.50 to 0.96).

705 When P_c is higher and fracture water desaturation occurs (e.g., > 100 kPa in this
706 study), the reduced capillary continuity of the fracture hinders water drainage from and
707 CO_2 invasion into the top matrix core. Thus matrix CO_2 saturation in Sample MP
708 decreases from 0.24 at a fracture water saturation of 0.50 in MP150, to 0.16 at a fracture
709 water saturation of 0.19 in MP200a, even when a higher P_c was applied to the latter (see
710 Figure 11). In MP150, the spatial and temporal changes in fracture water saturation vs.
711 matrix CO_2 saturation indicate the countercurrent flow of CO_2 and water at the fracture-
712 matrix interface. Compared to MP200b, the fracture water saturation, thus the capillary

713 continuity of the fracture and matrix CO_2 saturation were enhanced by (1) the non-
714 uniform CO_2-water distribution in the fracture, and (2) the lower capillary entry pressure
715 of matrix relative to portions of the fracture (see Section 3.2). The highest matrix CO_2
716 saturation presented in MP200b, when fracture water saturation and capillary pressure
717 increased simultaneously by reducing the circumferential surface of fracture available to
718 CO_2 invasion. Results from MP150, MP200a and MP200b indicate the complex CO_2-
719 water flow across the fracture-matrix interface, and the importance of fracture and matrix
720 properties (e.g., the capillary entry pressures) in determining CO_2-water flow in fractured
721 porous media.

722 In previous modeling work, we investigated the impacts of capillary
723 continuity/connectivity on CO_2 storage capacity and efficiency in meter scale stacked
724 columns (Bandilla et al., 2019). Numerical simulations were conducted on stacked
725 homogeneous matrix blocks with varying matrix-matrix connectivities at 0%, 30% and
726 100%. Modeling results showed no considerable difference of CO_2 saturation distribution
727 in the stacked columns for the cases of 30% and 100% matrix-matrix connectivities,
728 while significant difference in CO_2 saturation distribution was observed between the 0%
729 case and the 30 to 100% cases. Similar to the modeling results, we showed that when
730 capillary continuity determined by fracture water saturation is equal and over 0.3 (Case
731 MP150 and MP200a), CO_2 saturations in the top matrix are not considerably affected by
732 the fracture, whereas when the fracture water saturation is less than 0.3 (Case MP200b),
733 the matrix CO_2 saturation is greatly hindered over a longer period of time. Meanwhile,
734 our lab observations indicated a more complicated counter-current flow at the fracture-
735 matrix interface, as well as the pronounced impacts of matrix heterogeneity and

anisotropy. All these need to be considered for a more accurate predication of CO_2 storage efficiency. In addition, Ţene et al. (2017) investigated the two-phase flow in fractured porous media using a Projection-based Embedded Discrete Fracture Model (pEDFM), considering the fracture-matrix coupling terms by a cross-media transmissibility. Modeling results indicate the impacts of fracture positions and the cross-media conductivity contrasts. Kim et al. (2011) examined the experimental P_c-S_w functions of heterogeneous carbonate rock samples, and concluded that Leverett J-function cannot accurately describe the carbonate rocks due to heterogeneous pore systems with fractures and vugs. The X-ray CT images from this study directly visualized the dependence of CO_2-water flow and P_c-S_w functions on fractures and matrix, and indicated that single Leverett J-function may not be applicable in scaling P_c-S_w functions for field-scale studies, considering the orders of magnitude difference between fracture and matrix permeability.

At last, differing from the columns stacked with a single fracture (Samples HO, HP and MP), tests in Sample LO with multiple horizontal fractures present (1) the largest variations of CO_2 saturation within the core (Figure 11), and (2) the four fractures, orthogonal to the water drainage direction, served as conduits for CO_2 invasion at early time. They, however, hindered water drainage across and further CO_2 invasion from these fractures into neighboring matrix (Figure 10). These can be attributed to the increased water flow resistance (thus decreased water relative permeability) across the desaturated fractures. While the CO_2-water flow within a fracture or fracture network has been investigated by laboratory experiments and modeling (Shukla et al., 2010; Perera et al., 2011; Oh et al., 2013; Celia et al., 2015; March et al., 2018; Tao et al., 2019), cross-

759 fracture flow is worthy of a systematic and detailed investigation. Results from Sample
760 LO imply the spatial and temporal dependent role of fractures for 3-D CO_2-water flow,
761 the importance of fracture network (e.g., distribution, orientation, connectivities, and
762 transmissibility characteristics with respect to the matrix) in determining CO_2 distribution
763 and storage efficiency.

764 Common to all cases above is the observed higher CO_2 saturation at the bottom
765 portion of the matrix cores (1) in Samples HO and HP with high fracture continuity,
766 regardless of matrix anisotropy and applied P_c (e.g., Figure 5 and 6), and (2) in Samples
767 MP and LO, where fractures were desaturated and capillary continuity was considerably
768 reduced (Figures 7 and 10). This cannot be predicted by the dual-porosity approach that
769 assumes zero capillary continuity through the fracture (Warren and Root, 1963), or
770 observed by the classic core-flood experiments where confining pressure is applied and
771 CO_2-water flow is prohibited across the circumferential surface (Perrin and Benson,
772 2000; Krevor et al., 2012; Chang et al., 2013, 2014; Pini and Benson, 2013). In our
773 experiments, the 3-D displacement enables CO_2 invasion through the bottom fracture into
774 matrix and countercurrent water drainage from the matrix. This may benefit the fracture-
775 matrix flow and mass transfer and CO_2 storage efficiency in fractured reservoirs.

776 5. Conclusions and implications

777 Recent modeling results have demonstrated significant CO_2 storage efficiency in
778 fractured reservoirs when preferentially drained fractures retain certain
779 hydraulic/capillary continuity. In this study, we investigated the CO_2-water flow across an
780 mm-scale fracture and storage efficiency in rock matrix at room temperature and

781 controlled capillary pressures up to 200 kPa. Frequent X-ray CT scans provided direct
782 observations on the processes and show the importance of fracture capillary continuity
783 and fracture-matrix interactions. We observed the increase of displacement efficiency in
784 the matrix with increasing fracture water saturation (capillary continuity), and presented
785 that the fracture water saturations could be enhanced by the non-uniform fracture
786 capillary pressure and countercurrent flow of CO_2 and water across the fracture-matrix
787 interface. The displacement efficiency was also affected by matrix heterogeneity and
788 anisotropy, when high fracture water saturations (>0.6) were maintained. In naturally
789 fractured reservoirs, the interfacial tension of CO_2-water is expected to be considerably
790 lower than that under the experimental conditions in this study. In addition, fractures
791 develop with a wider range of apertures from microns to much larger, while individual
792 fractures may also contain spatially variable apertures (microns to millimeters). These
793 might collectively result in spatially variable and a larger span of capillary pressure
794 contrasts between fractures vs. matrix. While cautions are needed before applying the
795 experimental results to the field, this study implies that tight fractures and tight portions
796 of a rough fracture may sustain high water saturation, allowing for water drainage across
797 multiple matrix blocks and CO_2 invasion from large fractures. The cross-fracture flow of
798 water may bridge the preferentially drained fractures ahead of the CO_2 plume and
799 enhance CO_2 storage efficiency in matrix. In summary, adequate capillary continuity of
800 fractures and fracture-matrix interactions may result in continuous displacement that
801 occurs over multiple matrix blocks, to an extent that the single-block based dual porosity
802 model may greatly underestimate the CO_2 storage efficiency in fractured reservoirs.
803

Supporting Information (SI)

More detailed information on air permeability, contact angles and mineral compositions of the rock core samples, as well as the fitting parameters of the van Genuchten (1980) Model for both rock cores and the fracture are provided in the SI.

Notes

The authors declare no competing financial interest.

Acknowledgements

This material is based upon work supported by the U. S. Department of Energy and the Big Sky Regional Carbon Sequestration Partnership under Award Number DE-FC26-05NT42587. We appreciate the valuable comments provided by the reviewers and the Associate Editor, which helped improve presentation of this work.

References

Agada, S., Geiger, S. & Doster, F., 2016. Wettability, hysteresis and fracture-matrix interaction during CO_2 EOR and storage in fractured carbonate reservoirs. Int. J. Greenhouse Gas Control 46, 57–75.

Agarwal, R. G., Gardner, D. C., Kleinsteiber, S. W., Fussell, D. D., 1999. Analyzing well production data using combined type curve and decline curve concepts. SPE Reservoir Eval. Eng. 2 (5), 478e486. SPE-57916-PA.

Akin, S., Kovscek, A. R., 2003. in Applications of X-ray Computed Tomography in the Geosciences, ed. by Mees, F., Swennen, R., Van Geet, M., Jacobs, P. Geological Society, London, 215, 23–38.

Al-Menhali, A. S., Menke, H. P., Blunt, M. J., Krevor S. C., 2016. Pore scale observations of trapped CO_2 in mixed-wet carbonate rock: Applications to storage in oil fields. Environ. Sci. Technol. 50 (18), 10282–10290.

Arif, M., Lebedev, M., Barifcani, A., Iglauer, S., 2017. CO_2 storage in carbonates: Wettability of calcite. Int. J. Greenhouse. Gas Control 62, 113–121.

Aspenes, E., Ersland, G., Graue, A., Stevens, J., Baldwin, B. A., 2008. Wetting phase bridges establish capillary continuity across open fractures and increase oil recovery in mixedwet fractured chalk. Transp. Porous Media 74, 35–47.

Bandilla, K., Celia, M., Doster, F., Zhou, Q., 2019. Multiscale modeling of CO_2 migration and trapping in fractured reservoirs with validation by model comparison and real-site applications. DOE-Princeton-0023323, doi:10.2172/1496797.

Beckner, B. L., lshimoto, K., Yamaguchi, S., Firoozabadi, A., Aziz, A., 1987. Imbibition-

840 Dominated Matrix Fracture Transfer in Dual Porosity Simulators, paper SPE 16981
841 presented at the 1987 SPE Annual Technical Conference and Exhibition, Dallas, 27–
842 30 September.
843 Berg, S., Oedai, S., Ott, H., 2013. Displacement and mass transfer between saturated and
844 unsaturated CO_2-brine systems in sandstone. Int. J. Greenhouse Gas Control 12, 478–
845 492.
846 Bertels, S. P., DiCarlo, D. A., Blunt, M. J., 2001. Measurement of aperture distribution,
847 capillary pressure, relative permeability, and in situ saturation in a rock fracture using
848 computed tomography scanning. Water Resour. Res. 37 (3), 649–662.
849 Bogdanov, I. I., Mourzenko, V.V., Thovert, J. F., Adler, P. M., 2003. Two-phase flow
850 through fractured porous media. Phys. Rev. E 68, 026703.
851 Celia, M. A., Bachu, S., Nordbotten, J. M., Bandilla, K. W., 2015. Status of CO_2 storage
852 in deep saline aquifers with emphasis on modeling approaches and practical
853 simulations, Water Resour. Res. 51, 6846–6892.
854 Chang, C., Zhou, Q., Xia, L., Li, X., Yu, Q., 2013. Dynamic displacement and non-
855 equilibrium dissolution of supercritical CO_2 in low-permeability sandstone: An
856 experimental study. Int. J. Greenh. Gas Control 14, 1–14.
857 Chang, C., Zhou, Q., Guo, J., Yu, Q., 2014. Supercritical CO_2 dissolution and mass
858 transfer in low-permeability sandstone: Effect of concentration difference in water-
859 flood experiments. Int. J. Greenhouse Gas Control 28, 328–342.
860 Chang, C., Zhou, Q., Oostrom, M., Kneafsey, T. J., Mehta, H., 2017. Pore-scale
861 supercritical CO_2 dissolution and mass transfer under drainage conditions, Adv.
862 Water Resour., 100, 14–25.

Chun, B. S., Wilkinson, G. T., 1995. Interfacial tension in high-pressure carbon dioxide mixtures. Ind. Eng. Chem. Res. 34, 4371–4377.

Dane, J. H., Hopmans, J. W., 2002. Pressure Plate Extractor. In: Dane, J. H. and Topp, G.C., Eds., Methods of Soil Analysis: Physical Methods, Part 4, Soil Science Society of America, Madison, 688–690.

De la Porte, J. J., Kossack, C. A., Zimmerman, R. W., 2005. The effect of fracture relative permeabilities and capillary pressures on the numerical simulation of naturally fractured reservoirs. Paper presented at the SPE annual technical conference and exhibition, Dallas, Texas, USA, 9–12 Oct.

Dejam, M., Hassanzadeh, H., 2010. Formation of liquid bridges between porous matrix blocks. AIChE J. 57 (2), 286–298.

Festoy, S., Van Golf-Racht, T. D., 1989. Gas gravity drainage in fractured reservoirs through new dual-continuum approach. SPE Reservoir Eng. 4 (3), 271–278.

Fernø, M. A., Haugen, Å., Graue, A., 2011. Wettability effects on the matrix–fracture fluid transfer in fractured carbonate rocks. J. Petrol. Sci. Eng. 77 (1), 146–153.

Firoozabadi, A., 2000. Recovery mechanisms in fractured reservoirs and field performance. J. Can. Pet. Technol. 39 (11), 13–17.

Fletcher, R. C., Merino, E., 2001. Mineral growth in rocks: kinetic–rheological models of replacement, vein formation, and syntectonic crystallization. Geochim. Cosmochim. Acta 65, 3733–3748.

Gautam, P. S., Mohanty, K. K., 2004. Matrix–fracture transfer through countercurrent imbibition in presence of fracture fluid flow. Transp. Porous Media 55, 309–337.

Hermansen, H., Thomas, L. K., Sylte, J. E., Aasboe, B. T., 1997. Twenty-five years of Ekofisk reservoir management. In: SPE Annual Technical Conference and Exhibition San Antonio, Texas, 873–885.

Horie, T., Firoozabadi, A., Ishimoto, K., 1990. Laboratory studies of capillary interaction in fracture/matrix systems. SPE Res Eval. Eng. 5, 353–360.

Huo, D., Benson, S. M., 2016. Experimental investigation of stress-dependency ofrelative permeability in rock fractures. Transp. Porous Media 113, 567-590.

Ide, T. S., Jessen, K., Orr, F. M., 2007. Storage of CO_2 in saline aquifers: effects of gravity, viscous, and capillary forces on amount and timing of trapping. Int. J. Greenhouse Gas Control 1, 481–491.

Iding, M., and P. Ringrose (2010), Evaluating the impact of fractures on the performance of the In Salah CO 2 storage site, Int. J. Greenh. Gas Control, 4(2), 242–248.
Iding, M., and P. Ringrose (2010), Evaluating the impact of fractures on the performance of the In Salah CO 2 storage site, Int. J. Greenh. Gas Control, 4(2), 242–248.
Iding, M., Ringrose, P., 2010. Evaluating the impact of fractures on the performance of the In Salah CO_2 storage site, Int. J. Greenhouse Gas Control 4 (2), 242–248.

909 Jones, F. O., Owens, W. W., 1980. A laboratory study of low permeability gas sands. J.
910 Pet. Tech. 32, 1631–1640.
911 Kim, K.H., Lee, Y.S., Hwang, S.H., Seo, J., Sung, W., 2011. Improved capillary
912 pressuremodel considering dual-pore geometry system in carbonate reservoirs. J. Pet.
913 Sci. Eng. 78 (3–4), 601–608.
914 Klinkenberg, L., 1941. The Permeability of Porous Media to Liquids and Gases.
915 Drillingand Production Practice, American Petroleum Institute, New York.
916 Krevor, S. C. M, Pini, R., Zuo, L., Benson, S. M., 2012. Relative permeability and
917 trapping of CO_2 and water in sandstone rocks at reservoir conditions. Water Resour.
918 Res. 48 (2), W02532.
919 Lim, K., Aziz, K., 1995. Matrix-fracture transfer shape factors for dual-porosity
920 simulators. J. Pet. Sci. Eng. 13, 169–178.
921 Liu, H., Rutqvist, J., 2010. A new coal-permeability model: internal swelling stress and
922 fracture–matrix interaction. Transp. Porous Media 82, 157–171.
923 March, R., Doster, F., Geiger, S., 2018. Assessment of CO_2 storage potential in naturally
924 fractured reservoirs with dual-porosity models. Water Resour. Res. 54, 1650–1668.
925 Massoudi, R., King, A., 1974. Effect of pressure on the surface tension of water
926 adsorption of low molecular Weight Gases on Water at 25°. J. Phys. Chem. 78,
927 2262−2266.
928 Mirzaei, M., Das, D. B., 2007. Dynamic effects in capillary pressure–saturations
929 relationships for two-phase flow in 3D porous media: Implications of micro-
930 heterogeneities. Chem. Eng. Sci. 62, 1927−1947.
931 Morrow, N. R., Brower, K. R. Ma, S., Buckley, J. S., 1990. Fluid flow in healed tectonic

fractures, J. Pet. Technol. 42 (10), 1310–1318.

Narr, W., Schechter, D. S., Thompson, L. B., 2006. Naturally fractured reservoir characterization: Society of Petroleum Engineers.

Nelson, P. H., 2009. Pore–throat sizes in sandstones, tight sandstones, and shales: AAPG Bulletin, 93, 329–340.

Oh, J., Kim, K. Y., Han, W. S., Kim, T., Kim, J. C., Park, E., 2013. Experimental and numerical study on supercritical CO_2/brine transport in a fractured rock: Implications of mass transfer, capillary pressure and storage capacity. Adv. Water Res. 62, 442–453.

Peters, E. J. & Hardham, W. D., 1990. Visualization of fluid displacements in porous media using computed tomography imaging. J. Pet. Sci. Eng. 4, 155-168.

Peters, R. R., Klavetter, E. A., 1988. A continuum model for water movement in an unsaturated fractured rock mass. Water Resour. Res. 24, 416–430.

Pini, R., Madonna, C., 2016. Moving across scales: a quantitative assessment of X-ray CT to measure the porosity of rocks. J. Porous Mater 23, 325–338.

Pruess, K., Wang, J., Tsang, Y., 1990. On thermohydrologic conditions near high-level nuclear wastes emplaced in partially saturated fractured tuff: 1. Simulation studies with explicit consideration of fracture effects. Water Resour. Res. 26 (6), 1235–1248.

Pini, R., Benson S. M., 2013. Simultaneous determination of capillary pressure and relative permeability curves from core-flooding experiments with various fluid pairs. Water Resour. Res. 49, 3516–3530.

Perrin, J. C., Benson, S., 2009. An experimental study on the influenceof sub-core scale heterogeneities on CO_2 distribution in reservoir rocks, Transp. Porous Media 82 (1),

93–109.

Penuela, G., Hughes, R. G., Civan, F., Wiggins, M. L., 2002. Time dependent shape factors for secondary recovery in naturally fractured reservoirs. SPE 75234, SPE/DOE Improved Oil Recovery Symposium, Tulsa, Oklahoma, USA.

Perera, M. S. A., Ranjith P. G., Airey, D., Choi, S. K., 2011. Sub-critical and super-critical carbon dioxide flow behavior in naturally fractured black coal: An experimental study. Fuel 90(11), 3390-3397.

Ramsay, J. G., 1980. The crack-seal mechanism of rock deformation. Nature 284, 135–139.

Rangel-German, E. R., Kovscek, A. R., 2005. Matrix-fracture shape factors and multiphase-flow properties of fractured porous media. SPE 95105-MS, Presented at the SPE Latin American and Caribbean Petroleum Engineering Conference held in Rio de Janeiro, Brazil, 20–23 June.

Rangel-German, E. R., Kovscek, A. R., 2006. A micromodel investigation of two-phase matrix-fracture transfer mechanisms. Water Resour. Res. 42 (3), W03401.

Rangel-German, E., Akin, S., Castanier, L., 2006. Multiphase-flow properties of fractured porous media. J. Pet. Sci. Eng. 51, 197–213.

Parry W. T., 1998. Fault-fluid compositions fromfluid-inclusion observations and solubilities of fracture-sealing minerals. Tectonophysics 290, 1–26.

Reitsma, S., Kueper, B. H., 1994. Laboratory measurement of capillary pressure-saturation relationships in a rock fracture, Water Resour. Res. 30, 865–878.

Shi, J. Q., Xue, Z., Durucan, S., 2011. Supercritical CO_2 core flooding and imbibition in Tako sandstone-influence of sub-core scale heterogeneity, Int. J. Greenhouse Gas

Control, 5, 75–87.

Stones, E. J., Zimmerman, S. A., Chien, C. V., Marsden, S. S., 1992. The effect of capillary connectivity across horizontal fractures on gravity drainage from fractured porous media. SPE ATCE, Washington, D.C., USA.

Sulak, R. M., 1990. Ekofisk Field: The first 20 Years. SPE 20773, presented at the 1990 SPE annual Technical Conference and Exhibition, New Orleans, Sept. 23–26.

Shukla, R., Ranjith, P., Haque, A., Choi, X., 2010. A review of studies on CO_2 sequestration and caprock integrity. Fuel 89 (10), 2651−2664.

Tao, Y., Guo, B., Bandilla, K. W., Celia, M. A., 2019. Vertically integrated dual-continuum models for CO_2 injection in fractured geological formations. Comput. Geosci. 23273–23284.

Ţene, M., Bosma, S.B., Kobaisi, M.S.A., Hajibeygi, H., 2017. Projection-based embedded discrete fracture model (pEDFM). Adv. Water Resour. 105, 205–216.

Tokunaga, T. K., Shen, W., Wan, J., Kim, Y., Cihan, A., Zhang, Y., Finsterle, S., 2017. Water saturation relations and their diffusion-limited equilibration in gas shale: Implications for gas flow in unconventional reservoirs. Water Resour. Res. 53, 9757–9770.

Van Genuchten, M., 1980. A closed-form equation for predicting the hydraulic conductivity of unsaturated soils. Soil Sci. Soc. Am. J. 44, 892–898.

Warren, J. E., Root, P. J., 1963. The behavior of naturally fractured reservoirs. SPE J. 3, 245–55.

Wellington, S. L., Vinegar, H. J., 1987. X-ray computerized tomography, J. Pet. Technol. 39 (8), 885–898.

Xu, L., Myers, M., Li, Q., White, C., Zhang, X., 2020. Migration and storage characteristics of supercritical CO_2 in anisotropic sandstones with clay interlayers based on X-CT experiments. J. Hydrol. 580, 124239.

Zhao, H., Fedkin, M. V., Dilmore, R. M., Lvov, S. N., 2015. Carbon dioxide solubility in aqueous solutions of sodium chloride at geological conditions: Experimental results at 323.15, 373.15, and 423.15 K and 150 bar and modeling up to 573.15 K and 2000 bar. Geochim. Cosmochim. Acta 149, 165–189.

Zhou, Q., Oldenburg, C. M., Spangler, L. H., Birkholzer, J. T., 2017. Approximate solutions for diffusive fracture-matrix transfer: Application to storage of dissolved CO_2 in fractured rocks. Water Resour. Res. 53, 1746–1762.

Zhang, Y., Nishizawa, O., Kiyama, T., Chiyonobu, S., Xue, Z., 2014. Flow behaviour of supercritical CO_2 and brine in Berea sandstone during drainage and imbibition revealed by medical X-ray CT images. Geophys. J. Int. 197 (3), 1789–1807.

1015 Table 1 Properties of the core samples and ceramic plates used for the stacked columns

Samples and ceramic plates		#1 (HO)	#2 (HP)	Ceramic I	#3 (MP)	#4 (LO)	Ceramic II
Diameter×length (cm×cm)		5×10	5×10	5×0.7	5×10	5×9.5	5×0.7
Porosity		0.16	0.15	0.45	0.14	0.042	0.34
Absolute air permeability (mD)		46.00	5.32	/	0.167	0.17	/
Absolute water permeability (mD)		40	4.3	6.0	0.144	0.058	0.17
Capillary entry pressure (kPa)		13.8	13.8	100	135	135 (P1); 66 (P2)	300

CASE	P_c (kPa)	Fracture Water saturation	Matrix CO_2 saturation	Time to equilibrium (hrs)
Sample HO	HO20.7	20.7	0.93	0.38	102
	HO27.6	27.6	0.90	0.45	56
	HO41.4	41.4	0.80	0.56	145
	HO68.9	68.9	0.68	0.59	58
Sample HP	HP13.8	13.8	0.96	0.11	106.5
	HP41.4	41.4	0.80	0.50	43
Sample MP	MP150	150	*0.50**	0.24	216
	MP200a	200	0.19	0.16	>1222
	MP200b	200	*0.30**	0.36	>956
Sample LO	LO150	150	0.26	0.19	>701
	LO200	200	0.21	0.29	841

1017 Note: H, M, L = High, Medium, and Low permeability; O, P = bedding/fracture

1018 Orthogonal to, Parallel to the water drainage path.

1019 Table 2. The twelve water drainage experiments conducted with four core samples, and

1020 corresponding fracture water saturations, matrix CO_2 saturations and time to reach system

1021 equilibrium obtained by the end of each experiment.

1022

1023 Note: * indicates the observed fracture water saturations that deviate from the measured

1024 P_c-$S_{w,f}$ relation due to fracture-matrix interactions in MP150 and the reduced

1025 circumferential surface of fracture exposure to CO_2 in MP200b.

1026

1027